Dissociation of a Strong Acid in Neat Solvents: Diffusion is Observed after Reversible Proton Ejection inside the Solvent Shell.

Manoel Veiga-Gutiérrez,[†,¶] Alfonso Brenlla,[†,§] Carlos Carreira Blanco,[†] Berta Fernández,[†] Sergey A. Kovalenko,[‡] Flor Rodríguez-Prieto,[†] Manuel Mosquera,[*,†] and J. Luis Pérez Lustres[*,†]

Center for Research in Biological Chemistry and Molecular Materials (CIQUS), University of Santiago de Compostela, E-15782 Santiago de Compostela (Spain), and Institute of Chemistry, Humboldt University of Berlin, D-12489 Berlin (Germany)

E-mail: manuel.mosquera@usc.es; luis.lustres@usc.es

---

[*]To whom correspondence should be addressed
[†]CIQUS
[‡]HUB
[¶]now at PicoQuant GmbH, Kekuléstr. 7, 12489 Berlin (Germany)
[§]now at Department of Chemistry, Wayne State University, 5101 Cass Avenue, Detroit, MI 48202 (USA)

Abstract

Strong-acid dissociation was studied in alcohols. Optical excitation of the cationic photoacid N-methyl-6-hydroxyquinolinium triggers proton transfer to solvent, which was probed by spectral reconstruction of picosecond fluorescence traces. The process fulfills the classical Eigen–Weller mechanism in two stages: a) solvent-controlled reversible dissociation inside the solvent shell and b) barrierless splitting of the encounter complex. This can only be appreciated when fluorescence band integrals are used to monitor the time-evolution of reactant and product concentrations. Band integrals are insensitive to solvent dynamics and report relative concentrations directly. This was demonstrated by first measuring the fluorescence decay of the conjugate base across the full emission band and independently of the proton transfer reaction. Multiexponential decay curves at single wavelengths result from a dynamic red-shift of fluorescence in the course of solvent relaxation, whereas clean single exponential decays are obtained if the band integral is monitored instead. The extent of the shift is consistent with previously reported femtosecond transient absorption measurements, continuum theory of solvatochromism and molecular properties derived from quantum chemical calculations. In turn, band integrals show clean biexponential decay of the photoacid and triexponential evolution of the conjugate base in the course of the proton transfer to solvent reaction. The dissociation step follows the slowest stage of solvation, measured here independently by ps fluorescence spectroscopy in five aliphatic alcohols. Also, the rate constant of the encounter-complex splitting stage is compatible with proton diffusion. Thus, both stages reach for this photoacid the highest possible rates: solvation and diffusion control. In these conditions, the concentration of the encounter complex is substantial during the earliest nanosecond.

KEYWORDS: proton transfer, fluorescence spectroscopy, time-resolved spectroscopy, acids and bases, aqueous solution chemistry, kinetics, photochemistry.

Introduction

Intermolecular proton transfer is one of the most relevant processes in chemistry and biology.[1,2] The reaction involves three basic steps: diffusion of reactants to form an encounter complex, elementary proton transfer at collisional distances and subsequent diffusion of reaction products. The overall process may reach the diffusion-control limit when both reaction partners exhibit large enough differences in proton affinity. In that case, the reaction proceeds so swiftly that only ultrafast techniques succeed in probing kinetics at contact distances.[3–6]

Ultrafast electronic reorganization, solvent and hydrogen-bonding relaxation are concomitant to the primary proton transfer step.[7] But information about these processes is hard to obtain. They develop so rapidly that the reaction is necessarily controlled by much slower events like barrier crossing and/or diffusion. These limitations do not apply to photoinduced proton transfer to solvent (PTTS) reactions because reactants are already in contact when optical excitation starts the reaction. Ideally, all individual stages can be identified and traced by a combination of optical and vibrational time-resolved spectroscopies scanning reaction time delays from femtoseconds (fs) to nanoseconds (ns). Molecules which undergo ultrafast photoinduced PTTS reactions in proton-accepting solvents are termed *photoacids*.[8]

Photoacids show much lower pK_a in the excited electronic state than in the ground state. The pK_a may drop as much as 10 units upon electronic excitation.[3,9–11] Thus, optical excitation of the photoacid with a short laser pulse induces ultrafast photodissociation in proton-accepting solvents. As has been long recognized, electronic redistribution underlies the proton transfer process.[2,11,12] The rationale behind this effect is not unique. For instance, theoretical work by Granucci *el al.*[13] indicates that excited-state acidity of phenols and cyanophenols may be explained by charge redistribution in the deprotonated form only. The latter reduces the proton affinity of the conjugate base in the excited state. Spry and Fayer suggested that this behavior could be common to cationic photoacids.[14] In contrast, Stark spectroscopy of several neutral pyrene photoacids evidenced that the photoinduced charge shift depends on the electronic state being excited rather than the protonation state.[15] It means that optical charge redistribution "instantaneously" enhances acidity of

neutral photoacids.[14,15] Thus, strong photoacid behavior demands coupling of the PTTS reaction to intramolecular electronic redistribution.

Eigen's model for the dissociation of an acid in proton-accepting solvents is shown in Scheme 1.[1,7] Only strong photoacid behavior is discussed next. Proton donor and acceptor (the solvent) are in close contact when reaction starts. Photon absorption induces intramolecular charge redistribution at earliest time and thereby provides the driving force for dissociation inside the solvent shell. The process occurs typically in the femtosecond to picosecond timescales and is controlled by solvent dynamics.[3,9] Diffusion of products completes the reaction on a longer timescale.

The elementary dissociation step may occur in the quantum adiabatic and non-adiabatic limits for the proton coordinate, as proposed by Hynes and co-workers.[16] Note that electronic coupling is strong and the process is *electronically adiabatic*. In this picture the intrinsic proton transfer potential is modulated by the solvent and hydrogen bonding coordinates, *i.e.* proton transfer is an overall three-coordinate problem. Thus, the double-well proton transfer potential evolves under the influence of the solvent coordinate from an asymmetric double-well with global minimum in the AH^* form (reactant state) to the asymmetric potential of the product state, where the global minimum locates at the $A^* \cdots H^+$ form. In between, the transition state shows iso-energetic *diabatic* bound vibrational levels of the labile proton for AH^* and $A^* \cdots H^+$. Reaction free energies are constructed from the *diabatic* vibrational energies of reactant and product as function of the solvent coordinate, which is the true reaction coordinate. Proton transfer mirrors solvent relaxation in the adibatic limit, in which the transition state is characterized by vibrational wavefunctions of the bound proton extending over both potential wells. In turn, localized proton vibrational levels are the hallmark of the transition state in the nonadibatic limit. In this case, kinetics develops slower than solvation, even if the solvent coordinate continues to be the relevant reaction coordinate.

Final separation of the proton and the conjugate base occurs on the ps to ns timescales. The rate is controlled by diffusion and the stage may be reversible.[17] Pines and Huppert[18] reported geminate recombination[19] in pyranine (HPTS).[7,20,21] A general theory of geminate recombination was developed by Agmon.[7] The process applies generally, but it is however enhanced by strong

Coulombic interaction between the conjugate base and the proton, and may be best observed for long-lived charged reaction products.[22]

In short, elementary proton transfer and proton diffusion are the key elements of PTTS, Scheme 1. Both steps occur in overlapping timescales simultaneously with electronic redistribution and hydrogen bond reorganization. It is still a challenge to track all single processes individually via representative observables, which is essential even for the most qualitative understanding. Our contribution addresses exactly this point.

We analyzed PTTS for the photoacid N-methyl-6-hydroxyquinolinium (**C**). The process runs under solvation control, as demonstrated previously by fs transient absorption spectroscopy.[3] We now shift the focus to the diffusion stage in the ps to ns time range. The subject was already considered by the group of Solntsev in two recent publications,[9,23] where the geminate recombination model was assumed. This was analyzed with the application of Krissinel' and Agmon for solving Spherically-Symmetric Diffusion Problem (SSDP).[24] However, the program was adapted to account for the anisotropy of the interaction potential between the conjugate base and the proton and the effect of the counterion on proton mobility. An adequate force field was calculated by Brownian Dynamics simulations of the same photodissociation reaction.[23] The tailored SSDP program was then used to fit fluorescence traces measured in alcohols at different temperatures. Kinetic and thermodynamic parameters were deduced in this way.[9] We defend here a more heuristic approach.

Time-resolved fluorescence with ps time resolution and spectral reconstruction were applied together with solvatochromic shift analysis supported by high-level quantum chemical calculations. Reaction kinetics was monitored through the time-evolution of fluorescence band integrals instead of fluorescence traces at single wavelengths, because the latter still sense slowest stages of solvent dynamics. Proton transfer to the first solvent shell and diffusion were disentangled. The elementary dissociation step follows solvent relaxation and the proton remains, for the meantime, inside the shell. The process is reversible. Proton diffusion occurs on a slower timescale with no indication for geminate recombination in this case, as evidenced by clean exponential evolution of fluorescence band integrals.

Materials and Methods

Sample preparation and materials

N−methylquinolinium−6−olate (**Z**) and perchlorate of N−methyl−6−hydoxyquinolinium (**C**) were synthesized as described previously.[3,25] Corresponding chemical structures are shown in Scheme 1. Solutions were freshly prepared in spectroscopic grade (except 2-butanol and butyronitrile, 99.5% and 98%, respectively) non-degassed solvents from ALDRICH and SCHARLAU. Double distilled water was employed to prepare aqueous solutions, where the pH was set either to 4 or 9 by adding corresponding amounts of $HClO_4$ or NaOH. Typically, sample concentration was of the order of 10^{-4} M for steady-state absorption measurements and around 10^{-5} M for fluorescence. In femtosecond transient absorption the concentration was about 0.02 M. All solutions were passed through 0.22 μm filters (CAMEO). Photodegradation was observed in dimethylsulfoxide, dioxane and in acetone to a lesser extent. All measurements were conducted at room temperature, 22 °C. The list of abbreviations used for the solvents is included in the Supporting Information.

Absorption and fluorescence spectroscopy

Steady-state UV–vis absorption spectra were scanned in a VARIAN *Cary 3E* double-beam spectrophotometer. Fluorescence spectra were acquired in an SPEX *Fluorolog FL340 E1 T1* fluorometer at right angle geometry. Excitation and emission monochromators were calibrated with a Hg(Ar) pen-lamp (LOT ORIEL). The wavelength precisions of emission and excitation monochromators were better than 0.5 and 1 nm, respectively. Fluorescence spectra were corrected by the baseline of the solvent. Three to five independent scans were averaged. Resulting spectra were multiplied by correction functions obtained by the method of Gardecki and Maroncelli.[26] Fluorescence emission spectra were further multiplied by λ^4 to convert the fluorescence quantum distribution over wavelengths into cross-section of stimulated emission (σ_{SE}). Stimulated emission was chosen because it is the proper counterpart of the absorption lineshape,[27] so that absorption and emission spectra can be compared quantitatively.

Fluorescence decay curves were measured by the time-correlated single photon counting technique (TC-SPC) in an EDINBURGH INSTRUMENTS *LifeSpec-ps* time-resolved spectrofluorometer. The system is equipped with a diode laser as excitation source (PICOQUANT LDH-P-C-375 controlled by a PDL 800-B unit, $\lambda_{max} = 371$ nm, maximum repetition rate 40 MHz, 60 ps FWHM and $10 - 30$ pJ/pulse). A microchannel plate photomultiplier (HAMAMATSU *R3809U-50*) with 50 ps response time and detection range of $200 - 850$ nm was used as detector. The repetition rate of the excitation source was set to 2.5 MHz and 4000 counts were acquired in the maximum at counting rates of less than 125 kHz. The multichannel analyzer (MCA) has 4096 channels with minimum width of 0.61 ps/channel. Magic angle polarization was employed. The instrument response function (≈ 100 ps FWHM) was obtained by monitoring the scattered light at the most intense Raman band of the corresponding solvent.

All steady-state absorption and fluorescence measurements were done in 1 cm-thick fused-silica cuvettes and slit widths were chosen so that acceptable signal-to-noise ratios were reached: 2 nm of absorption, 8 nm for fluorescence and 16 nm for TC-SPC.

Pump-supercontinuum probe (PSCP) measurements

The pump-supercontinuum probe setup employed to measure fs transient absorption was described in reference 25 and a comprehensive account of the PSCP technique was published elsewhere.[28] Briefly, basic pulses were delivered by a regenerative Ti:Sa amplifier (CLARK MXR, *CPA-2001*, 0.9 mJ/pulse, 150 fs, 120 Hz). They were used to pump a non-collinear optical parametric amplifier (NOPA) tuned to 540 nm (≈ 25 fs, 10 μJ). The 540 nm pulses were split for red-edge optical pumping of the **Z** form and for white-light continuum generation. The supercontinuum was filtered and split for reference before being imaged onto the sample cell (spot size ≈ 100 μm and 0.4 mm thickness). Transmitted and reference beams were further imaged onto the entrance planes of separate homemade prism spectrographs and registered by photodiode arrays with 512 pixels (HAMAMATSU *S3901-512Q*). The average spectral resolution at the position of the stimulated emission band of **Z** was 3 nm (about 100 cm^{-1} in this wavelength range). Measurements

7

were performed at parallel and perpendicular polarizations and one transient spectrum represents the average of 50 consecutive shots. Transient spectra were acquired with constant step-size. Step-sizes ranging from 2 to 200 fs steps were employed and four independent scans were averaged. Pump-probe cross-correlation was estimated by the non-resonant coherent solvent signal. The average cross-correlation FWHM was found to be 60 fs across the full spectral window. Transient spectra were corrected for the chirp of the supercontinuum. PSCP measurements were performed in methanol and ethanol only.[25]

Quantum chemical calculations

Hartree-Fock (HF), Density Functional Theory (DFT) with the B3LYP functional (denoted B3LYP in the following) and second order Møller–Plesset Perturbation theory (MP2) ab initio methods were used for geometry optimization of **Z** in the ground electronic state. Dunning's correlation consistent polarized valence cc-pVTZ and aug-cc-pVTZ basis sets were employed. Calculations were carried out with the program packages Gaussian 09[29] and DALTON.[30]

The number of significant figures quoted is indicative of the fit uncertainties or measurement precision.

Results

Solvatochromism and Proton Transfer to Solvent. Absorption and stimulated emission (SE) spectra of **C** are shown in Figure 1, Frame A. The absorption spectrum is characterized by two bands with maxima at 350 and 315 nm. The position of these bands is practically independent of solvent polarity. In turn, the emission spectrum (here and from now on shown as SE cross-section, σ_{SE}) depends markedly on solvent properties. In acetonitrile (ACN), the emission band shows up at 450 nm. In aqueous solution at pH=4, a new emission band appears at $\approx$ 600 nm while a weak shoulder persists at 450 nm. The excitation spectra measured in both emission bands are the same, which demonstrates that they originate from the same species in the ground electronic state. As

shown in a previous publication,[3] the bands monitor emission of the cationic $\mathbf{C}^*$ and neutral $\mathbf{Z}^*$ forms, *i.e.* $\mathbf{C}^*$ dissociates in the first excited singlet state in protic solvents.

Optical spectra of $\mathbf{Z}$ are shown in Figure 1, Frame B. The first absorption band shifts to the blue by ≈ 5000 cm^{-1} upon increasing solvent polarity, as measured by the polarity parameter $\Delta f(\varepsilon, n^2) = \dfrac{\varepsilon - 1}{\varepsilon + 2} - \dfrac{n^2 - 1}{n^2 + 2}$.[31–33] ε and n are the dielectric constant and refractive index of the solvent, respectively. For instance, the absorption peak position is 19465 cm^{-1} in ethyl acetate but shifts to 24380 cm^{-1} in water. A similar trend is observed for the cross-section of SE but the shift is less pronounced in this case. Therefore, the Stokes shift rises towards higher polarity. Note however that the Stokes shift is 5295 cm^{-1} in ACN but 7675 cm^{-1} in methanol (MeOH) despite the similar Δf values shown by both solvents. Overall, the solvatochromic shift is consistent with a decrease of the $\mathbf{Z}$ molecular dipole moment upon optical excitation to the S_1 state. Deviations between protic and non-protic solvents of similar polarity (Δf) suggest hydrogen-bonding interactions contributing to the solvatochromic shift.

Figure 2 shows the $\mathbf{Z}^*$ fluorescence decay curves measured in ethanol (EtOH) across the full emission band. These results complete and are consistent with those published by Gould *et al.* in Reference 9. The fluorescence decay is multiexponential and depends strongly on the emission wavelength. A multiexponential global fit performed for 23 emission wavelengths yielded decay times of 4 ps, 39 ps, 1.20 ns together with a minor component of 5.97 ns in EtOH.[34] The associated amplitudes of the shortest decay times (mainly 39 ps) are positive in the blue flank of the spectrum and become increasingly negative in the red wing ($640 - 720$ nm). Similar results are obtained for other alcohols: methanol (MeOH), 1-propanol (PrOH), 2-butanol (2BuOH) and 1-octanol (OcOH) although decay times vary significantly among the different alcohols. This behavior is consistent with a dynamic red-shift of the $\mathbf{Z}^*$ fluorescence emission band.

The fluorescence decay curves were used to reconstruct the time evolution of the SE cross-section of $\mathbf{Z}^*$, Figure 3, according to the procedure outlined in the literature.[35–38] Shortly, the decay curves were deconvoluted and the response functions $I_R(\lambda, t)$ were integrated analytically in time for each wavelength: $I(\lambda) = \int_{band} I_R(\lambda, t)dt \approx \sum_{i=1}^{m} a_i(\lambda)\tau_i$. m is the number of exponential

functions and $a_i(\lambda)$ are the amplitudes associated to the decay times τ_i at the emission wavelength λ. The ratio $\chi(\lambda) = \dfrac{\sigma_{SE}(\lambda)}{I(\lambda)}$ is calculated and used to multiply each response function $I_R(\lambda,t)$. The empirical correction factor $\chi(\lambda)$ accounts for the wavelength-dependent difference between spontaneous and SE bandshapes and for instrumental spectral sensitivity. The product $\chi(\lambda) \times I_R(\lambda,t)$ provides the SE signal at delay time t and discrete wavelengths λ. The time-dependent SE bandshape $\sigma_{SE}(\lambda,t)$ is approximated by a *log-normal* fit at each delay time, Figure 3. When monitored with ps TC-SPC, the SE shifts to the red by few hundred reciprocal centimeters ($\approx$ 150 cm^{-1} in EtOH) at early time and decays afterwards with constant bandshape. The small ($\approx$ 150 cm^{-1}) red shift resolved in Figure 3 explains the complex wavelength-dependent fluorescence decay shown in Figure 2. In turn, reconstructed band integrals of stimulated emission show clean monoexponential decay (see Supporting Information, Figure SI 2).

A similar procedure was applied to reconstruct the time-evolution of the SE spectrum of $\mathbf{C}^*$ in EtOH, Figure 4. $\mathbf{C}$ may be excited selectively in alcohols if the HClO$_4$ concentration is above 10^{-5} M. Consistent with previous observations,[3] a significant part of the SE cross-section stems from the neutral form $\mathbf{Z}^*$. This means that PTTS occurs to a substantial extent during the earliest 10 ps delay and remains unresolved in the measurements described here.[39] This very early stage of the PTTS reaction was studied previously by fs PSCP.[3] Slower stages are addressed now by ps TC-SPC.

PSCP spectra of $\mathbf{Z}^*$ in EtOH are shown in Figure 5 for 540 nm excitation. The transient spectra present the negative signatures of bleach and SE together with the positive contribution of excited-state absorption (ESA). During the earliest two picoseconds, bleach and ESA stay constant while the SE band shifts to the red by $\approx$ 1000 cm^{-1}.[3,25] This behavior was assigned to solvation dynamics. It is shown here to quantify the spectro-temporal resolution of the TC-SPC experiment and guide characterization of solvent dynamics in alcohols with longer aliphatic chains.

Quantum mechanical calculations. The molecular structure of the $\mathbf{Z}$ form was calculated with HF, B3LYP and MP2 methods. Geometries optimized at the HF and B3LYP levels differ significantly but this is not the case when the latter are compared to MP2 results. The differences between

the geometrical parameters calculated with the cc-pVTZ and the aug-cc-pVTZ basis sets with B3LYP are on the third decimal for the bond distances and on the first for the angles. Therefore, we considered the B3LYP/cc-pVTZ and B3LYP/aug-cc-pVTZ optimized geometries and evaluated for both the ground state electrical properties. A summary of these results is included in the Supporting Information (Tables SI 1 to SI 5).

Electric dipole moments (μ) and isotropic polarizabilities (α) calculated for **Z** in the ground electronic state are summarized in Table 1 and in the Supporting Information (Tables SI 1 and SI 2).[40,41] B3LYP properties are considerably closer to MP2 than HF. For instance, $\mu_0 = 9.994$ D at the MP2/cc-pVTZ level but 10.542 D at B3LYP and 12.070 D at HF with the same basis. It was observed that augmentation of the basis set is not needed for geometry optimization, but it makes a significant contribution to the electrical properties (B3LYP differences up to 2.6% for μ and 7.3% for α). Therefore, electrical properties calculated at the B3LYP/aug-cc-pVTZ level of theory were selected for solvatochromic shift analysis.

Considering the above, the first-excited singlet-state geometry was also optimized with the B3LYP method and the aug-cc-pVTZ basis set. Electrical properties were calculated at the same level, Table 1. Dipole moments were found to be collinear in both electronic states and are therefore hereafter used as scalar quantities. Ground and excited state B3LYP/aug-cc-pVTZ optimized geometries are included in the Supporting Information (Tables SI 3 to SI 5).

Discussion

This section is organized as follows: first, the stationary solvatochromic shifts of the **Z** form are analyzed in light of dielectric continuum theory of solvation for a polarizable point dipole with electric molecular properties obtained by high-level quantum chemical calculations. The Stokes shift is split into instantaneous and orientational solvation contributions. The latter is essential for estimating the time-zero fluorescence spectrum and to determine characteristic solvation times $\langle \tau_{solv} \rangle$ in alcohols. Furthermore, the kinetic components associated with pure solvation dynamics

of the **Z** form are identified. They hinder direct mapping of concentration evolution by means of fluorescence traces at single wavelengths.[42] Stimulated emission band integrals remain in turn unaffected. We analyze next time-resolved emission spectra obtained upon ps excitation of **C** in alcohols and we find two regimes for the PTTS reaction. An early stage occurs in the fs timescale and is controlled by solvent dynamics.[3,9] This stage accounts for $> 50\%$ of the reaction and remains largely unresolved in the ps experiment. In the second stage, slower decay of the $\mathbf{C}^*$ emission band and concomitant rise of the $\mathbf{Z}^*$ band is observed. The rate constant is consistent with diffusion control. It implies that a substantial part of the dissociation reaction occurs in a dynamic but closed solvent shell.[42–44]

Polar Solvatochromic Shift of Z

The analysis presented in this subsection aims to measure the dynamic solvation shift of **Z**, to determine the characteristic solvation times in alcohols and to estimate the peak position of the $\mathbf{Z}^*$ SE band at time-zero. An accurate method based on the spectral shift and broadening of steady-state spectral data in non-polar solvents was proposed by Maroncelli and co-workers.[45] The method cannot be applied here because **Z** is essentially not soluble in non-polar solvents. Instead, we opt for modeling the solvatochromic shift with the classical dielectric continuum theory of solvation. The so-obtained orientational contribution is added to the stationary SE frequency to assess the peak position at time zero.

The solvatochromic shift of **Z** is summarized and analyzed in Figure 6, where $\Delta\tilde{\nu}_{Stokes}$ is the Stokes shift and $\tilde{\nu}_{max}$ is either the absorption or SE peak position. The negative solvatochromism is clearly recognized in absorption and emission spectra as an increase of the transition energy with the solvent polarity parameter $\Delta f(\varepsilon, n^2) = \dfrac{\varepsilon - 1}{\varepsilon + 2} - \dfrac{n^2 - 1}{n^2 + 2}$. Note however that the solvatochromic shift is steep in protic solvents (alcohols, empty squares) but much more modest in non protic ones (filled squares). The behavior expected for point polarizable dipoles sitting at the center of a spherical cavity of radius a and immersed in a dielectric continuum with static dielectric constant ε and refractive index n is given by the McRae equations:[33,46]

$$\tilde{v}_{abs} = \tilde{v}^{\circ}_{abs} + \Delta\tilde{v}^{disp} + \frac{2}{hc}\frac{\mu_0^2 - \mu_1^2}{a^3}f(n^2) + \frac{2}{hc}\frac{\mu_0(\mu_0 - \mu_1)}{a^3}\Delta f(\varepsilon, n^2)$$
$$+ \frac{6}{hc}\frac{\mu_0^2(\alpha_0 - \alpha_1)}{a^6}\Delta f^2(\varepsilon, n^2) \tag{1a}$$

$$\tilde{v}_{SE} = \tilde{v}^{\circ}_{SE} + \Delta\tilde{v}^{disp} + \frac{2}{hc}\frac{\mu_0^2 - \mu_1^2}{a^3}f(n^2) + \frac{2}{hc}\frac{\mu_1(\mu_0 - \mu_1)}{a^3}\Delta f(\varepsilon, n^2)$$
$$+ \frac{6}{hc}\frac{\mu_1(5\mu_1 - 2\mu_0)(\alpha_0 - \alpha_1)}{a^6}\Delta f^2(\varepsilon, n^2) \tag{1b}$$

$$\Delta\tilde{v}_{Stokes} = \Delta\tilde{v}^{\circ}_{Stokes} + \frac{2}{hc}\frac{(\mu_0 - \mu_1)^2}{a^3}\Delta f(\varepsilon, n^2)$$
$$+ \frac{6}{hc}\frac{[(\mu_0 + \mu_1)^2 - 6\mu_1^2](\alpha_0 - \alpha_1)}{a^6}\Delta f^2(\varepsilon, n^2) \tag{1c}$$

In Equations (1) μ_i and α_i are the dipole moments and polarizabilites of the electronic state i, h is the Planck constant and $\circ$ indicates the value of the superscripted magnitude in the gas phase. Briefly, $\Delta\tilde{v}^{disp}$ and $\frac{2}{hc}\frac{\mu_0^2 - \mu_1^2}{a^3}f(n^2)$ depend linearly on $f(n^2) = \frac{n^2 - 1}{2n^2 + 1}$ and report the instantaneous frequency shift by dispersion and dipole–induced dipole solute–solvent interactions, respectively. The two instantaneous interactions account for the tiny solvatochromic shift observed in non-polar solvents, the so-called *non-polar shift*, which is the same for absorption and emission. In the usual approach, the non-polar shift is quantified in non-polar solvents only and is then subtracted from the actual peak position observed in polar and non-polar solvents. The desired orientational part remains. It provides dipole moments and polarizabilities for ground and excited states for a given cavity radius a. An alternative method is however needed because of the poor solubility of **Z** in non-polar solvents.

We concentrate on alcohols. Dipole moments and isotropic polarizabilities were replaced in Equations (1) with the values found by quantum chemical calculations (Table 1). The gas-phase Stokes shift and the absorption peak positions were fitted together with the cavity radius a by a non-linear least squares routine. Note that the dispersion contribution is considered together with the gas-phase peak positions. This implicitly assumes that $\Delta\tilde{v}_{disp}$ is small and approximately constant for solvents with similar refractive indexes, as is nearly the case for linear aliphatic alcohols. The

absorption peak position was fitted first. Optimal values are: $\tilde{\nu}_{abs}^{\circ} + \Delta\tilde{\nu}_{disp} = 16900 \pm 2400$ cm^{-1} and $a = 4.0 \pm 0.5$ Å. a is consistent with the molecular size of **Z**, but this parameter is not well defined for non-spherical molecules like **Z**. Consequently, a is just the radius for which the continuum model best mimics the actual polar solute-solvent interactions. Eventually, a may even capture small deviations due to specific hydrogen-bonding interactions. We fixed $a = 4$ Å in the fits of the the SE peak positions and the Stokes shift, so that gas-phase values are obtained with better precision. Optimization yields $\Delta\tilde{\nu}_{Stokes}^{\circ} = 5040 \pm 300$ cm^{-1} and $\tilde{\nu}_{fl}^{\circ} + \Delta\tilde{\nu}_{disp}$ of 12040 ± 200 cm^{-1} (Figure 6). The fit is reasonably good, despite hydrogen-bonding interactions. Absorption and fluorescence bands deviate less than ± 500 cm^{-1} from the continuum prediction, our spectral resolution being 200 cm^{-1}. Larger deviations are observed for the Stokes shift in water, MeOH and 2BuOH and we will come to this point later. The extrapolated gas-phase peak positions corrected by dispersion interactions are blue-shifted by $\approx 500 - 700$ cm^{-1} compared to those derived from quantum mechanical calculations: $\tilde{\nu}_{abs}^{\circ} = 16400$ cm^{-1} and $\tilde{\nu}_{fl}^{\circ} = 11300$ cm^{-1}. This suggests that: a) dispersion interactions have a minor contribution to solvatochromic shift, probably in the range of 500 cm^{-1} and b) hydrogen bonding energy is very close for ground- and first-excited singlet states. If b) were not true, slopes of solvatochromic shifts would depart clearly from the prediction of dielectric continuum theory in hydroxylic solvents,[47] contrary to observation.

It is conceivable that the < 700 cm^{-1} deviations observed for the Stokes shift in water and MeOH arise from hydrogen-bonding interactions. In support, Allolio and Sebastiani calculated in a recent study[48] that the **Z**$\cdots$H$_2$O hydrogen bond weakens significantly upon excitation in water but the associated reorganization energy (λ_{HB}) is less than 1 mHartree. Thus, the maximum limit for the hydrogen-bonding contribution to the Stokes shift is $2\lambda_{HB} \leq 400$ cm^{-1}. The latter should be even smaller in long chain linear alcohols. Therefore, the small contribution of hydrogen-bonding reorganization is parameterized by the cavity radius a, which has strong influence over the slope of the solvatochromic shift.[49]

Next, the SE peak position at time zero, $\tilde{\nu}_{SE}(0)$, is estimated by evaluation of the orientational solvation contributions: dipole–dipole and induced dipole–dipole. These are calculated with

the corresponding terms in Equations (1), where the optimized cavity radius a and the electric molecular properties (μ_i and α_i) calculated by B3LYP were used. $\tilde{\nu}_{SE}(0)$ equals the sum of the steady-state SE energy and the orientational shift, Figure 6 and Table 3. The method reports dynamic Stokes shifts of 3410 and 3170 cm^{-1} in water and MeOH, respectively, consistent with experimental values: 3050 and 2850 cm^{-1} by fs PSCP in the same solvents[3,25] and 3130 cm^{-1} by broadband fluorescence up-conversion in water.[41,50][51] Thus, we conclude that continuum theory explains *semiquantitatively*, within ± 500 cm^{-1}, the solvatochromic shift of **Z** in hydroxylic solvents.

We finish this section with a short remark about the solvatochromism in non-protic polar solvents. Unexpectedly, no solvatochromic shift is observed. This contrasts with the semiquantitative and consistent picture provided by continuum theory in alcohols and water. We can only conjecture that this effect arises from specific hydrogen-bonding interactions with water traces in the non-protic solvent but no clear-cut justification can be advanced at present.

Characteristic Solvation Times in Alcohols

We discuss now the dynamic red-shift of the **Z*** emission band. A band shift of a few hundred cm^{-1} is resolved by ps fluorescence spectroscopy in aliphatic alcohols (Figure 3). The extent of the spectral displacement is solvent dependent. Thus, the observed shift is ≈ 100 and 150 cm^{-1} in MeOH and EtOH but reaches 800 cm^{-1} in OcOH. This is however a (small) part of the fluorescence red-shift previously deduced for solvent orientational relaxation, Table 3 and Figure 6.

Figure 7 compares the fluorescence red-shift measured in MeOH and EtOH by broadband fs transient absorption and ps fluorescence. Transient absorption monitors the SE band directly, while the peak position is obtained by spectral reconstruction in fluorescence measurements. The latter were vertically shifted by a small amount δ for better overlap between both sets of data at long delays. δ is well within the spectral resolution of the TC-SPC experiment. About 70% of the dynamic solvation shift could be resolved by fs transient absorption. The solvation correlation function is constructed by combining the time-zero peak position from solvatochromic analysis with the time-

dependent peak position measured by fs transient absorption, $C(t) = \dfrac{\tilde{v}_{SE}(t) - \tilde{v}_{SE}(\infty)}{\tilde{v}_{SE}(0) - \tilde{v}_{SE}(\infty)}$. The latter monitors the position in the solvation coordinate, $z(t)$.[52] In contrast, ps TC-SPC artificially red-shifts the SE band for time delays shorter than the FWHM of the TC-SPC instrument response.[45] Note however that both curves overlap precisely at longer delays, where the SE peak position can be measured faithfully by spectral reconstruction of ps fluorescence data. It means that only the latest $\approx 10\%$ of the solvent displacement occurs in the ps timescale in MeOH and EtOH but $z(t)$ could still evolve from 0.6 to 1 (equilibrium) in this timescale in viscous alcohols, see below. An important consequence of this observation is that fluorescence decay curves measured in alcohols with sub-100 ps pulses still sense spectral shifts induced by solvent dynamics, despite limited time resolution. This effect is strong enough to prevent direct mapping of excited-state population evolution from time-dependent fluorescence signals measured at single wavelengths. The observation is distorted by the underlying spectral dynamics.

The fs-resolved SE peak positions in Figure 7 were fitted with multiexponential functions, Table 4. The characteristic solvation time $\langle \tau_{solv} \rangle$ is calculated as $\langle \tau_{solv} \rangle = \displaystyle\int_0^\infty C(t)dt = \sum_{i=1}^{n} a_i \tau_i$, where $C(t)$ is the solvation correlation function, n is the number of exponential functions with decay times τ_i employed in the fit of $C(t)$ and a_i are the relative amplitudes associated to each exponential i. We measured $\langle \tau_{solv} \rangle$ values of 2.8 and 6.1 ps in MeOH and EtOH, respectively, when the orientational solvent contribution is taken into account.[3,37,47,50] This contrasts with the slowest components of solvation τ_{slow} determined in this work by ps fluorescence in the same solvents: 21 and 39 ps. Despite this, τ_{slow} can be combined with SE peak positions at time-zero to define an interval enclosing $\langle \tau_{solv} \rangle$: $\tau_{slow} > \langle \tau_{solv} \rangle > a_{slow}\tau_{slow}$. a_{slow} is determined by the ratio between the SE shift decaying with τ_{slow} and the full solvation shift, $a_{slow} = \dfrac{\tilde{v}_{SE}^{SPC}(0) - \tilde{v}_{SE}(\infty)}{\tilde{v}_{SE}(0) - \tilde{v}_{SE}(\infty)}$.

Table 4 summarizes the characteristic solvation times obtained in this work. MeOH and EtOH were characterized with highest accuracy. The time constants are in line with previous reports.[3,37,47,50] $\langle \tau_{solv} \rangle$ deviates by not more than a factor of 2 from the longitudinal times $\tau_L = \varepsilon_\infty / \varepsilon_0 \tau_D$, where ε_0 is the static dielectric constant of the solvent, ε_∞ is the high-frequency limit of the frequency-dependent dielectric constant and τ_D is the Debye relaxation time.[53] Only the slow-

est Debye relaxation time is considered, although dielectric dispersion is best represented by 2-3 Debye terms in alcohols. ε_∞ is calculated as $\approx 1.1 n_D^2$, where n_D is the refractive index at sodium D-line. For all other alcohols, for which fs measurements are not available, solvation times are characterized by τ_L and the limits defined by τ_{slow} and $a_{slow}\tau_{slow}$, Figure 8.

Picosecond proton transfer to solvent

Figure 4 shows the time evolution of the fluorescence spectrum measured after ps optical excitation of the **C** form in EtOH. The spectra were reconstructed from fluorescence decays measured at single wavelengths. Earliest ps spectra show a significant amount of the $\mathbf{Z}^*$ form, consistent with the fact that dissociation occurs to a large extent on an ultrafast timescale.[3] ps evolution shows further decay of the $\mathbf{C}^*$ band and rise of the $\mathbf{Z}^*$ band. The latter decays within few ns. Slow stages of the proton transfer to solvent reaction are analyzed next.

The emission spectra reconstructed in Figure 4 were decomposed into $\mathbf{C}^*$ and $\mathbf{Z}^*$ bands by non-linear least squares fits performed at each delay time. Log-normal lineshapes were assumed. The method reports time-dependent peak positions and the band integrals. The $\mathbf{Z}^*$ peak position mirrors the redshift observed for $\mathbf{Z}^*$ alone and can be definitely assigned to solvation dynamics. Consequently, fluorescence decays measured in the blue and red flanks of the bands show decay and rise components associated with the underlying spectral dynamics, Figure 2.[3,9,42] In turn, band integrals are void from this artifact. Besides, the oscillator strength f_{osc} of the $S_1 \rightarrow S_0$ transition is proportional to the SE band integral. Therefore, band integrals report the relative excited-state concentrations of reactant and product because both transitions bear similar oscillator strength in this case.

The time-dependent $\mathbf{C}^*$ and $\mathbf{Z}^*$ SE band integrals are shown in Figure 9 and SI 4 for the proton transfer reaction to EtOH. The $\mathbf{Z}^*$ form accounts for about 70% of the signal at time zero. The concentrations of $\mathbf{C}^*$ and $\mathbf{Z}^*$ decay and rise concomitantly. Strikingly, the data are best explained by biexponential decay of $\mathbf{C}^*$ and triexponential time evolution of $\mathbf{Z}^*$ with two rise components. Rate constants of 26.7 and 5.8 ns^{-1} fit simultaneously the decay of $\mathbf{C}^*$ and the rise kinetics of $\mathbf{Z}^*$.

The latter decays with a 1.19 ns time constant, which coincides with the fluorescence lifetime of $\mathbf{Z}^*$ in ethanol (1.20 ns) as determined by independent measurements of fluorescence band integrals (see Figure SI 2 in Supporting Information). Essentially the same behavior is observed in MeOH, deuterated ethanol (EtOD), PrOH, 2BuOH and OcOH (see Table 5 and Figures SI 2 and SI 5 in the Supporting Information).

Biexponential decay of the excited cation can only be explained by reversible dynamics.[42] A trivial mechanism by which two sub-populations of $\mathbf{C}^*$ dissociate at different rates also complies with observations but can be regarded as unlikely. Also, it may be argued that biexponential decay of the cation reflects solvent dynamics, which is multiexponential and controls the dissociation stage. This is also unlikely because solvation dynamics is monoexponential in the ps timescale in all the alcohols investigated, except OcOH (Figure SI 2 in Supporting Information). Therefore, reversible dynamics is considered. Triexponential evolution of $\mathbf{Z}^*$ demands an intermediate stage as proposed in Scheme 2. The reaction proceeds as follows: solvation controls the intrinsic proton transfer step with characteristic rate constant k_1.[3] Note that the ps experiment probes the later stages of solvation only, *i.e.* ultrafast components of solvation explain non-zero concentration of $\mathbf{Z}^*$ at time zero and thus, k_1 corresponds to the "tail" of the solvent response.[3,9,10,23] The primary dissociation step is assumed to be reversible with a rate constant k_{-1}. The encounter complex $\mathbf{Z}^* \cdots \mathrm{H}^+$ may deactivate to the ground electronic state via k_Z or split with a rate constant k_2. The latter process could, in principle, be reversible[42] but we found no indication for that, as the small concentrations of protons and $\mathbf{Z}^*$ could anticipate.

The rate equations derived for the mechanism in Scheme 2 were integrated analytically[54] with the definitions in Equations (2). The resulting time-dependent concentrations are collected in Equations (3). Associated amplitudes were shifted to the Supporting Information. Note that, for simplicity, $\mathbf{P}^*$ refers to the encounter complex while $\mathbf{F}^*$ denotes the free $\mathbf{Z}^*$ molecules, *i.e.* those for which the proton has already abandoned the first solvation shell. $\mathbf{P}^*$ and $\mathbf{F}^*$ have the same spectral properties at the spectral resolution of the ps measurements but different time evolution. Therefore, the band integral of $\mathbf{Z}^*$ is calculated as the sum of those of $\mathbf{P}^*$ and $\mathbf{F}^*$. To account for the

non-resolved stages of the reaction, non-zero initial concentrations of $\mathbf{C}^*$ and $\mathbf{P}^*$ were assumed.

$$X = k_1 + k_C \tag{2a}$$

$$Y = k_2 + k_Z + k_{-1} \tag{2b}$$

$$Z = \sqrt{(X-Y)^2 + 4k_1 k_{-1}} \tag{2c}$$

$$\beta_1 = \frac{1}{2}(X+Y+Z) \tag{2d}$$

$$\beta_2 = \frac{1}{2}(X+Y-Z) \tag{2e}$$

$$[\mathbf{C}^*](t) = A_1^C \exp(-\beta_1 t) + A_2^C \exp(-\beta_2 t) \tag{3a}$$

$$[\mathbf{P}^*](t) = A_1^P \exp(-\beta_1 t) + A_2^P \exp(-\beta_2 t) \tag{3b}$$

$$[\mathbf{F}^*](t) = A_1^F \exp(-\beta_1 t) + A_2^F \exp(-\beta_2 t) + A_3^F \exp(-k_Z t) \tag{3c}$$

$$[\mathbf{Z}^*](t) = [\mathbf{P}^*](t) + [\mathbf{F}^*](t) = A_1^Z \exp(-\beta_1 t) + A_2^Z \exp(-\beta_2 t) + A_3^Z \exp(-k_Z t) \tag{3d}$$

The deduced time-dependent concentrations fit the data remarkably well when the amplitudes are calculated by solving the overdetermined system of linear equations in the least-squares sense, Figure 9. Optimal values of β_1, β_2 and k_Z^{-1} are shown in Table 5 for all solvents investigated. Also remarkable, the global fit is not significantly worse when the amplitudes are restricted to the values predicted by the model in Scheme 2 (Equations (3), Equations SI 3 in the Supporting Information and Figure 9). This is quite a strong condition, which enables the calculation of the $\mathbf{P}^*$ and $\mathbf{F}^*$ transient concentrations. Interestingly, most of the molecules remain encapsulated in the solvent shell for the earliest 500 ps. In viscous solvents, like OcOH, about 50% of the $\mathbf{Z}^*$ emission stems from the encounter complex (Supporting Information, Figure SI 5).

We can now operate with β_1, β_2 and k_Z to obtain the unknown rate constants k_1, k_{-1} and k_2. The assumption is made that $k_1 + k_2 + k_Z \gg k_{-1}$. This is justified by the small contribution

of the second exponential in the decay of $\mathbf{C}^*$, *i.e.* the elementary proton transfer stage is nearly irreversible. Consequently, $\beta_1 + \beta_2 \approx k_1 + k_2 + k_Z$ and $\beta_1 \times \beta_2 = k_1(k_2 + k_Z)$. Since k_Z is known by independent measurements of $\mathbf{Z}^*$ fluorescence decay (Supporting Information, Figure SI 2), k_1 and k_2 can be obtained precisely. Resulting values are collected in Table 5. We first note that k_1^{-1} is almost coincident with the slowest solvation component, as assumed by the kinetic model[3] (Tables 4 and 5). Next, we observe that $\tau_2 = k_2^{-1}$ shows typical values of a diffusion-controlled reaction, depends linearly on solvent viscosity η and is much longer than the corresponding solvation times (Figure 10).[17,55,56] We analyze τ_2 in terms of hydrodynamic diffusion theory.

According to the model in Scheme 2, k_2 is the splitting rate of the encounter complex. We assume that the process is barrierless and occurs in the diffusion-control limit. Therefore k_2 must be proportional to D, which is the mutual diffusion coefficient of $\mathbf{Z}^*$ and H^+, Equations (4).[55] D is approximated as D_H only because of the smaller radius of the proton compared to that of $\mathbf{Z}^*$. The diffusion coefficient is estimated via the Stokes-Einstein expression for classical hydrodynamic flow of spherical particles in non-slip conditions, Equations (4). R^* is the on-contact center-to-center distance between $\mathbf{Z}^*$ and the proton, while ΔV is the volume of the spherical shell surrounding $\mathbf{Z}^*$ and accommodating the proton. Therefore, a linear fit of $\tau_2 = k_2^{-1}$ versus solvent viscosity provides the geometrical parameter $\dfrac{R^*}{\Delta V R_H}$, where R_H is the radius of the excess proton.

$$k_2 = 4\pi D \frac{R^*}{\Delta V} \tag{4a}$$

$$D = D_Z + D_H \approx D_H = \frac{kT}{6\pi R_H \eta} \tag{4b}$$

The thickness of the spherical shell may be estimated semiquantitatively by assuming that $R_Z \approx 4$ Å, as deduced previously by analysis of solvatochromic shifts. A thickness of about 4 Å is deduced. In other words, the average $O \cdots O$ distance in the $\mathbf{Z}^* \cdots H^+ \cdots O(H) - R$ hydrogen bond is about 4 Å in alcohols. In support, Marx et al. calculated a $O \cdots O$ distance of 2.8 Å for non-centrosymmetric hydrogen bonds established between two water molecules sharing a proton

in aqueous solution.[57] This means that $O \cdots O$ shows the right order of magnitude, although the estimate is certainly too crude for quantitative analysis of the hydrogen bond strength in the solvent shell.

We close this section with a remark about water, where no dynamics could be observed in the ps timescale. This is not due to lack of time resolution because diffusion in water proceeds only slightly faster than in MeOH, where ps dynamics was clearly observed (Figure 10). It follows that the PTTS reaction occurs irreversibly in a closed solvent shell, *i.e.* before diffusion sets in. By the end of solvent relaxation, all molecules are in the $\mathbf{Z}^* \cdots H^+$ form, which is obviously not distinguishable from free $\mathbf{Z}^*$ by optical spectroscopy.

Summarizing, the classical Eigen–Weller mechanism in Scheme 2 successfully explains the time-evolution of band integrals and is fully consistent with independent measurements of characteristic rate constants of solvation and proton diffusion. Contrary to earlier reports about the same photoacid,[9,23] we find no signature of geminate recombination *outside* the solvent shell. Thus, non-exponential dynamics suggesting spatially inhomogeneous proton concentration is not observed when stimulated emission band integrals are used to probe PTTS dynamics in N-methyl-6-hydroxyquinolinium. The latter is deduced for N-methyl-6-hydroxyquinolinium specifically. We explicitly state that neither the geminate recombination model nor the experimental data in References 23 and 9 are here questioned. Activation energies for the PTTS reaction are expected to be semiquantitative correct and we also surmise that this photoacid is the strongest reported to date.[3,9,11] However, geminate recombination is difficult to justify in this case and this obviously casts some doubts about the accuracy of the rate constants deduced under the assumption of this model. It is here demonstrated that correction for dynamic contributions associated to solvent dynamics exposes the clean exponential evolution of concentrations in the sub-ns timescale and evidences significant transient concentrations of the encounter complex.

The encounter complex has been formally proposed by Eigen as an elusive reaction intermediate in the course of proton transfer to solvent reactions.[1] Its role has been emphasized by several authors since then.[42–44,58,59] The measurements here described provide firm experimental evidence

for the encounter complex and define the conditions under which it could be interrogated by spectroscopic methods.

Conclusions

We have analyzed proton transfer from a cationic photoacid to alcohols. The reaction presents two consecutive stages: dissociation inside the solvent shell and subsequent proton diffusion, Scheme 2.

An effort was made to characterize the dynamic solvation shift of the deprotonated form quantitatively. The study provides characteristic solvation times, evidences the charge-transfer character of the electronic transitions associated to photoacid behavior and shows that hydrogen-bond reorganization follows the solvent coordinate adibatically.[47] An important consequence is that fluorescence kinetic traces measured at single wavelengths with ps resolution are unsuitable to probe proton transfer dynamics directly: they just distinguish the rapid redshift of the emission band in the course of solvent relaxation. Proton transfer to solvent occurs simultaneously. In turn, fluorescence band integrals monitor reaction dynamics faithfully and provide the relative concentrations of reactant and product.

Multi-exponential decay of excited cation and zwitterion reveals reversible dissociation in the solvent shell and subsequent proton diffusion. Early dissociation occurs in the adiabatic limit[16] and is controlled by solvent dynamics.[3] The small contribution of a second exponential in the decay of the acid indicates a faint back reaction. The rate constant could not be determined accurately, but it probably lies between 0.1 and 1 ns^{-1} to compete with excited-state deactivation and diffusion out of the solvent shell.

The reaction products occur in two forms: hydrogen bonded inside the reaction shell (Eigen's encounter complex) and free. The two forms can be disentangled by their characteristic kinetic behavior rather than by distinct fluorescence signals. It is deduced that, in this particular case, the encounter complex is predominant during the earliest ns in fluid solvents and may be the only

emitting species in highly viscous media. This opens the door to structural characterization of the encounter complex by high-resolution ultrafast Raman spectroscopy.[60] Our results corroborate the Eigen–Weller proton transfer mechanism.[1]

Acknowledgement

Supporting Information Available

Ground and excited-state gas-phase geometries of N-methylquinolinium-6-olate, dipole moments, molecular axes and atom numbering. Summary of electrical properties calculated at different levels of theory in the ground and first-excited state. Complete analytical expressions for the concentrations of the intervening species in the mechanism of Scheme 2. Fluorescence band integrals of N-methylquinolinium-6-olate in alcohols. Global multiexponential fit of time-resolved fluorescence of C* in ethanol. Logarithmic representation of reaction kinetics in ethanol. Reaction kinetics in 1-octanol. Abbreviations of solvents employed. Full reference of Gaussian 09. This material is available free of charge via the Internet at http://pubs.acs.org/.

References

(1) (a) Eigen, M. Proton Transfer, Acid-Base Catalysis, and Enzymatic Hydrolysis. Part I. Elementary processes. *Angew. Chem. Int. Edit.* **1964**, *3*, 1–19; (b) Eigen, M.; Kruse, W.;

Maass, G.; Demaeyer, L. Rate Constants of Protolytic Reactions in Aqueous Solution. *Prog. React. Kinet. Mech.* **1964**, *2*, 285–289; (c) Eigen, M. Kinetics of Proton Transfer Processes. *Discuss. Faraday Soc.* **1965**, *39*, 7–15; (d) Beens, H.; Grellmann, K. H.; Gurr, M.; Weller, A. H. Effect of Solvent and Temperature on Proton Transfer Reactions of Excited Molecules. *Discuss. Faraday Soc.* **1965**, *39*, 183–193.

(2) Bell, R. P. *The Proton in Chemistry*; Chapman and Hall, 1973.

(3) Perez-Lustres, J. L.; Rodriguez-Prieto, F.; Mosquera, M.; Senyushkina, T. A.; Ernsting, N. P.; Kovalenko, S. A. Ultrafast Proton Transfer to Solvent: Molecularity and Intermediates from Solvation- and Diffusion-Controlled Regimes. *J. Am. Chem. Soc.* **2007**, *129*, 5408–5418.

(4) Rini, M.; Magnes, B.-Z.; Pines, E.; Nibbering, E. T. J. Real-Time Observation of Bimodal Proton Transfer in Acid-Base Pairs in Water. *Science* **2003**, *301*, 349–352.

(5) Siwick, B. J.; Cox, M. J.; Bakker, H. J. Long-Range Proton Transfer in Aqueous Acid-Base Reactions. *J. Phys. Chem. B* **2008**, *112*, 378–389.

(6) Cox, M. J.; Bakker, H. J. Femtosecond Study of the Deuteron-Transfer Dynamics of Naphtol Salts in Water. *J. Phys. Chem. A* **2010**, *114*, 10523–10530.

(7) Agmon, N. Elementary Steps in Excited-State Proton Transfer. *J. Phys. Chem. A* **2005**, *109*, 13–35.

(8) Tolbert, L.; Solntsev, K. Excited-State Proton Transfer: From Constrained Systems to "Super" Photoacids to Superfast Proton Transfer. *Acc. Chem. Res.* **2002**, *35*, 19–27.

(9) Gould, E.-A.; Popov, A. V.; Tolbert, L. M.; Presiado, I.; Erez, Y.; Huppert, D.; Solntsev, K. M. Excited-State Proton Transfer in N-Methyl-6-Hydroxyquinolinium Salts: Solvent and Temperature Effects. *Phys. Chem. Chem. Phys.* **2012**, *14*, 8964–8973.

(10) Kim, T. G.; Topp, M. R. Ultrafast Excited-State Deprotonation and Electron Transfer in Hydroxyquinoline Derivatives. *J. Phys. Chem. A* **2004**, *108*, 10060–10065.

(11) Bardez, E.; Chatelain, A.; Larrey, B.; Valeur, B. Photoinduced Coupled Proton and Electron Transfers. 1. 6-Hydroxyquinoline. *J. Phys. Chem.* **1994**, *98*, 2357–2366.

(12) Bardez, E.; Fedorov, A.; Berberan-Santos, M. N.; Martinho, J. M. G. Photoinduced Coupled Proton and Electron Transfers. 2. 7-Hydroxyquinolinium Ion. *J. Phys. Chem. A* **1999**, *103*, 4131–4136.

(13) Granucci, G.; Hynes, J. T.; Millie, P.; Tran-Thi, T. H. A Theoretical Investigation of Excited-State Acidity of Phenol and Cyanophenols. *J. Am. Chem. Soc.* **2000**, *122*, 12243–12253.

(14) Spry, D. B.; Fayer, M. D. Charge Redistribution and Photoacidity: Neutral versus Cationic Photoacids. *J. Chem. Phys.* **2008**, *128*, 084508.

(15) Silverman, L. N.; Spry, D. B.; Boxer, S. G.; Fayer, M. D. Charge Transfer in Photoacids Observed by Stark Spectroscopy. *J. Phys. Chem. A* **2008**, *112*, 10244–10249.

(16) Kiefer, P. M.; Hynes, J. T. Theoretical Aspects of Tunneling Proton Transfer Reactions in a Polar Environment. *J. Phys. Org. Chem.* **2010**, *23*, 632–646.

(17) Caldin, E. F. *The Mechanisms of Fast Reactions in Solution*; IOS Press, 2001.

(18) Pines, E.; Huppert, D. Geminate Recombination Proton-Transfer Reactions. *Chem. Phys. Lett.* **1986**, *126*, 88–91.

(19) Noyes, R. M. Kinetics of Competitive Processes when Reactive Fragments are Produced in Pairs. *J. Am. Chem. Soc.* **1955**, *77*, 2042–2045.

(20) Elsaesser, T., Bakker, H. J., Eds. *Ultrafast Hydrogen Bonding Dynamics and Proton Transfer Processes in the Condensed Phase*; Understanding Chemical Reactivity; Kluwer Academic Publishers: P.O. Box 17, 3300 AA Dordrecht, The Netherlands, 2002; Vol. 23.

(21) Tran-Thi, T. H.; Gustavsson, T.; Prayer, C.; Pommeret, S.; Hynes, J. T. Primary Ultrafast Events Preceding the Photoinduced Proton Transfer from Pyranine to Water. *Chem. Phys. Lett.* **2000**, *329*, 421–430.

(22) Presiado, I.; Karton-Lifshin, N.; Erez, Y.; Gepshtein, R.; Shabat, D.; Huppert, D. Ultrafast Proton Transfer of Three Novel Quinone Cyanine Photoacids. *J. Phys. Chem. A* **2012**, *116*, 7353–63.

(23) Popov, A. V.; Gould, E.-A.; Salvitti, M. A.; Hernandez, R.; Solntsev, K. M. Diffusional Effects on the Reversible Excited-State Proton Transfer. From Experiments to Brownian Dynamics Simulations. *Phys. Chem. Chem. Phys.* **2011**, *13*, 14914–14927.

(24) Krissinel', E. B.; Agmon, N. Spherical Symmetric Diffusion Problem. *J. Compt. Chem.* **1996**, *17*, 1085–1098.

(25) Perez Lustres, J. L.; Kovalenko, S. A.; Mosquera, M.; Senyushkina, T.; Flasche, W.; Ernsting, N. P. Ultrafast Solvation of N-Methyl-6-Quinolone Probes Local IR Spectrum. *Angew. Chem., Int. Ed.* **2005**, *44*, 5635–5639.

(26) Gardecki, J. A.; Maroncelli, M. Set of Secondary Emission Standards for Calibration of the Spectral Responsivity in Emission Spectroscopy. *Appl. Spectrosc.* **1998**, *52*, 1179–1189.

(27) Birks, J. B. In *Photophysics of Aromatic Molecules*; Birks, J. B., Ed.; Wiley Monographs in Chemical Physics; Wiley Interscience, 1970.

(28) (a) Dobryakov, A. L.; Kovalenko, S. A.; Weigel, A.; Perez-Lustres, J. L.; Lange, J.; Mueller, A.; Ernsting, N. P. Femtosecond Pump/Supercontinuum-Probe Spectroscopy: Optimized Setup and Signal Analysis for Single-Shot Spectral Referencing. *Rev. Sci. Instrum.* **2010**, *81*, 113106; (b) Kovalenko, S. A.; Dobryakov, A. L.; Ruthmann, J.; Ernsting, N. P. Femtosecond Spectroscopy of Condensed Phases with Chirped Supercontinuum Probing. *Phys. Rev. A* **1999**, *59*, 2369–2384.

(29) Frisch, M. J. et al. Gaussian 09 Revision A.1. Gaussian Inc. Wallingford CT 2009.

(30) DALTON, a Molecular Electronic Structure Program, Release 2.0 (2005), see http://www.kjemi.uio.no/software/dalton/dalton.html.

26

(31) von Lippert, E. Dipolmoment und Elektronenstruktur von Angeregten Molekulen. *Z. Natur-forsch. A* **1955**, *10*, 541–545.

(32) von Lippert, E. Habilitationsschrift zur Erlangung der Lehrberichtigung (venia Legendi) für das Fach Physikalische Chemie an der Techischen-Hochschule-Stuttgart – Spektroskopische Bestimmung des Dipolmomentes Aromatischer Verbindungen im Ersten Angeregten Sin-gulettzustand. *Z. Elektrochem.* **1957**, *61*, 962–975.

(33) Mataga, N.; Kubota, T. *Molecular Interactions and Electronic Spectra*; Marcel Dekker, Inc.: New York, 1970.

(34) The 5.97 ns decay time stems from an impurity. Its contribution is small but noticeable around 500 nm because of the small fluorescence quantum yield of the $\mathbf{Z}^*$ form and its swift fluorescence redshift. Fluorescence decays measured recently in purified samples did not show this contribution.

(35) O'Connor, D. V.; Phillips, D. *Time-Correlated Single Photon Counting*; Academic Press: New York, 1984.

(36) Kahlow, M. A.; Jarzeba, W.; Kang, T. J.; Barbara, P. F. Femtosecond Resolved Solvation Dynamics in Polar-Solvents. *J. Chem. Phys.* **1989**, *90*, 151–158.

(37) Horng, M. L.; Gardecki, J. A.; Papazyan, A.; Maroncelli, M. Subpicosecond Measurements of Polar Solvation Dynamics – Coumarin-153 Revisited. *J. Phys. Chem.* **1995**, *99*, 17311–17337.

(38) (a) Gardecki, J. A.; Maroncelli, M. Comparison of the Single-Wavelength and Spectral-Reconstruction Methods for Determining the Solvation-Response Function. *J. Phys. Chem. A* **1999**, *103*, 1187–1197; (b) Gardecki, J.; Horng, M. L.; Papazyan, A.; Maroncelli, M. Ul-trafast Measurements of the Dynamics of Solvation in Polar and Nondipolar Solvents. *J. Mol. Liq.* **1995**, *65-6*, 49–57; (c) Chapman, C. F.; Fee, R. S.; Maroncelli, M. Measurements of the

Solute Dependence of Solvation Dynamics In 1-propanol – the Role of Specific Hydrogen-Bonding Interactions. *J. Phys. Chem.* **1995**, *99*, 4811–4819.

(39) The areas of the $\mathbf{C}^*$ and $\mathbf{Z}^*$ bands are approximately proportional to the excited state concentrations of both species provided that the oscillator strengths of their $S_1 \rightarrow S_0$ transitions are comparable.

(40) Allolio, C.; Sajadi, M.; Ernsting, N.; Sebastiani, D. An Ab-Initio Microscope: Water H-Bonding and Reorientational Contributions to the Femtosecond Time-Dependent Fluorescence Shift of a Reichardt-Type Dye. *Angew. Chem., Int. Ed.* **2013**, *52*, 1813–1816.

(41) Sajadi, M.; Ajaj, Y.; Ioffe, I.; Weingaertner, H.; Ernsting, N. P. Terahertz Absorption Spectroscopy of a Liquid Using a Polarity Probe: A Case Study of Trehalose/Water Mixtures. *Angew. Chem., Int. Ed.* **2010**, *49*, 454–457.

(42) Spry, D. B.; Goun, A.; Fayer, M. D. Deprotonation Dynamics and Stokes Shift of Pyranine (HPTS). *J. Phys. Chem. A* **2007**, *111*, 230–237.

(43) Leiderman, P.; Genosar, L.; Huppert, D. Excited-State Proton Transfer: Indication of Three Steps in the Dissociation and Recombination Process. *J. Phys. Chem. A* **2005**, *109*, 5965–5977.

(44) Gepshtein, R.; Leiderman, P.; Genosar, L.; Huppert, D. Testing the Three Step Excited State Proton Transfer Model by the Effect of an Excess Proton. *J. Phys. Chem. A* **2005**, *109*, 9674–9684.

(45) (a) Fee, R. S.; Milsom, J. A.; Maroncelli, M. Inhomogeneous Decay Kinetics and Apparent Solvent Relaxation at Low-Temperatures. *J. Phys. Chem.* **1991**, *95*, 5170–5181; (b) Maroncelli, M.; Fee, R. S.; Chapman, C. F.; Fleming, G. R. Dynamic Stokes Shift In Coumarin - Is It Only Relaxation - Comment. *J. Phys. Chem.* **1991**, *95*, 1012–1014; (c) Fee, R. S.; Maroncelli, M. Estimating the Time-zero Spectrum in Time-resolved Emission Measurements of Solvation Dynamics. *Chem. Phys.* **1994**, *183*, 235–247.

(46) McRae, E. G. Theory of Solvent Effects on Molecular Electronic Spectra. Frequency Shifts. *J. Phys. Chem.* **1957**, *61*, 562–572.

(47) Sajadi, M.; Obernhuber, T.; Kovalenko, S. A.; Mosquera, M.; Dick, B.; Ernsting, N. P. Dynamic Polar Solvation Is Reported by Fluorescing 4-Aminophthalimide Faithfully Despite H-Bonding. *J. Phys. Chem. A* **2009**, *113*, 44–55.

(48) Allolio, C.; Sebastiani, D. Approaches to the Solvation of the Molecular Probe N-Methyl-6-Quinolone in its Excited State. *Phys. Chem. Chem. Phys.* **2011**, *13*, 16395–16403.

(49) Indeed, *a* is slightly larger than previously reported (3.5 Å)[25] but still physically meaningful. For instance, the calculated ground-state O−H (methyl) distance is 7.4 Å, which indicates a cavity radius larger than 3.7 Å when the van der Waals radii of both atoms are taken into account.

(50) Sajadi, M.; Weinberger, M.; Wagenknecht, H.-A.; Ernsting, N. P. Polar Solvation Dynamics in Water and Methanol: Search for Molecularity. *Phys. Chem. Chem. Phys.* **2011**, *13*, 17768–17774.

(51) Thermochromic shifts of steady-state spontaneous fluorescence also support the $\tilde{v}_{SE}(0)$ estimates: the emission band shifts to the blue by 3300 cm^{-1} in 2BuOH upon lowering the temperature from 298 to 160 K, close to the freezing point (158.5 K). Unpublished results.

(52) Van der Zwan, G.; Hynes, J. T. Time-dependent Fluorescence Solvent Shifts, Dielectric Friction, and Nonequilibrium Solvation In Polar-solvents. *J. Phys. Chem.* **1985**, *89*, 4181–4188.

(53) Marcus, Y. *The Properties of Solvents*; Wiley Series in Solution Chemistry; Wiley, 1998; Vol. 4; p 239.

(54) Eigen, M.; Maeyer, L. D. In *Techniques of Organic Chemistry*; Friess, S. L., Lewis, E. S., Weissberger, A., Eds.; Interscience: New York, 1963; Vol. 8; Chapter 18.

(55) (a) Perrin, C. L. "Diffusion-Controlled" Unimolecular Reactions and the Lifetime of a Strong Acid in Water. *J. Am. Chem. Soc.* **1986**, *108*, 6807–6808; (b) Astumian, R. D.; Schelly, Z. A. Explicit Consideration of the Excluded Volume in the Formula for Diffusion-Controlled Dissociation Rate Constants. *J. Phys. Chem.* **1986**, *90*, 537–538.

(56) Strehlow, H. *Rapid Reactions in Solution*; VCH Verlagsgesellschaft mbH, 1992.

(57) Marx, D.; Tuckerman, M. E.; Hutter, J.; Parrinello, M. The Nature of the Hydrated Excess Proton in Water. *Nature* **1999**, *397*, 601–604.

(58) Wang, S.; Bianco, R.; Hynes, J. T. An Atmospherically Relevant Acid: HNO_3. *Comput. Theor. Chem.* **2011**, *965*, 340–345.

(59) Thomas, V.; Maurer, P.; Iftimie, R. On the Formation of Proton-Shared and Contact Ion Pair Forms during the Dissociation of Moderately Strong Acids: An Ab Initio Molecular Dynamics Investigation. *J. Phys. Chem. B* **2010**, *114*, 8147–8155.

(60) Kovalenko, S. A.; Dobryakov, A. L.; Ernsting, N. P. An Efficient Setup for Femtosecond Stimulated Raman Spectroscopy. *Rev. Sci. Instrum.* **2011**, *82*, 063102.

Tables

Table 1: Molecular electrical properties of Z obtained from quantum chemical calculations at the B3LYP//aug-cc-pVTZ level in the ground and first-excited singlet state. Geometries were optimized by the same method in the indicated state.

state	μ_0/ D	μ_1/D	$\bar\alpha_0$/Å^3	$\bar\alpha_1$/Å^3
S_0	10.542		22.34	
S_1		7.326		20.08

Table 2: Gas-phase peak positions and Stokes shifts of Z obtained by applying dielectric continuum theory of solvatochromism to protic solvents only. Results from quantum chemical calculations are shown for comparison.

solvent type	$\tilde\nu^\circ_{abs}$/cm^{-1}	$\tilde\nu^\circ_{SE}$/cm^{-1}	$\Delta\tilde\nu^\circ_{Stokes}$/cm^{-1}	μ_0/ D	μ_1/ D
theoretical	16400	11300	5100	10.5	7.3
protic (polarizable model)	16900	12040	5040		

Table 3: Stationary and time-zero stimulated emission peak positions of Z together with the dynamic Stokes shift (all in cm^{-1}) from solvatochromic shift analysis with dielectric continuum theory of dipolar solvation.

solvent	$\tilde\nu_{fl}(\infty)$	$\tilde\nu_{fl}(0)$	$\tilde\nu_{fl}(0) - \tilde\nu_{fl}(\infty)$
water	16350	19755	3405
MeOH	15605	18770	3165
EtOH	15555	18485	2930
PrOH	15530	18290	2760
BuOH	15355	17975	2620
2BuOH	15575	18165	2590
iBuOH	15410	18055	2645
HeOH	15360	17725	2365
HpOH	15390	17625	2235
OcOH	15600	17710	2110

Table 4: Multiexponential fits to dynamic solvation shifts of stimulated emission. Decay times (τ_i) and associated amplitudes (a_i) for the normalized $C(t)$ function. The time zero spectrum was estimated from the analysis of solvatochromic shifts in protic solvents. The superscript ^{G} indicates a gaussian function rather than an exponential. (ps) or (fs) refer to ps fluorescence or fs transient absorption data published in this work. Longitudinal times (τ_L) are indicated for each solvent. Literature values for the same probe and for coumarin 153 (C153) are quoted for comparison.

probe/solvent	τ_1 /ps	a_1	τ_2 /ps	a_2	τ_3 /ps	a_3	τ_4 /ps	a_4	$\langle\tau_{solv}\rangle$ /ps	τ_L /ps
MeOH										3.1
Z/MeOH (fs)	0.05^G	0.32	0.41	0.25	2.8	0.25	12	0.17	2.8	
Z/MeOH (ps)							21	0.03	0.6-21	
Z/MeOH[3]			0.11	0.29	2.7	0.31	26	0.40	11	
C153/MeOH[37]	0.03	0.10	0.28	0.34	3.2	0.30	15	0.26	5.0	
EtOH										12
Z/EtOH (fs)	0.04^G	0.58	0.32	0.25	2.8	0.17	21	0.38	6.1	
Z/EtOH (ps)							39	0.06	1.9-39	
Z/EtOH[3]			0.31	0.36	4.3	0.27	26	0.37	11	
C153/EtOH[37]	0.03	0.09	0.39	0.23	5.0	0.18	30	0.50	16	
PrOH										44
Z/PrOH (ps)							68	0.10	7-68	
C153/PrOH[37]	0.03	0.09	0.34	0.17	6.6	0.23	48	0.52	26	
2BuOH										65
Z/2BuOH (ps)							77	0.18	14-77	
OcOH										295
Z/OcOH (ps)					34	0.11	215	0.34	77-172	

Table 5: Parameters obtained from a global fit of the C* and Z* band integrals (β_1, β_2 and k_Z^{-1}) and calculated values of k_1^{-1} and k_2^{-1} (see text). The fluorescence lifetime of Z* (τ_Z) was measured independently (Figure SI 2) and compared to the fitted values of k_Z^{-1}. The slowest solvation component τ_{slow} is also shown for comparison with k_1^{-1}.

solvent	β_1 / ns^{-1}	β_2 / ns^{-1}	k_Z^{-1} / ns	τ_Z / ns	k_1^{-1} / ps	τ_{slow} / ps	k_2^{-1} / ps
MeOH	39.0	13.9	1.17	1.18	26	21	77
EtOH	26.7	5.8	1.19	1.20	38	39	202
EtOD	29.7	6.9	1.44	1.47	34		162
PrOH	22.6	5.3	1.26	1.24	44	68	222
2BuOH	16.7	2.3	1.25	1.23	60	77	663
OcOH	6.7	1.4	1.45	1.12	148	172	1520

Floats

Eigen's Mechanism for Proton Transfer to Solvent
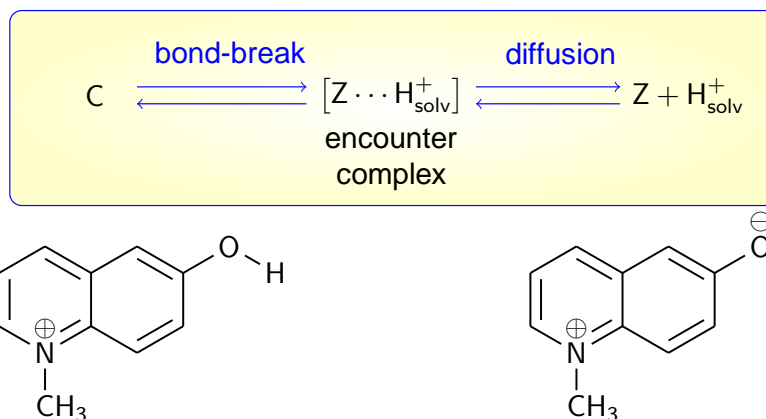
Scheme 1: Eigen's model for the proton transfer reaction from an acid C to the solvent (upper panel). Reactants are already in contact when the proton transfer to solvent reaction starts. Elementary stages are shown in blue and the encounter complex is indicated specifically. Molecular structures of the photoacid $N-$methyl$-6-$hydroxyquinolinium (**C**) and the conjugate base $N-$methylquinolinium$-6-$olate (**Z**) are shown below.
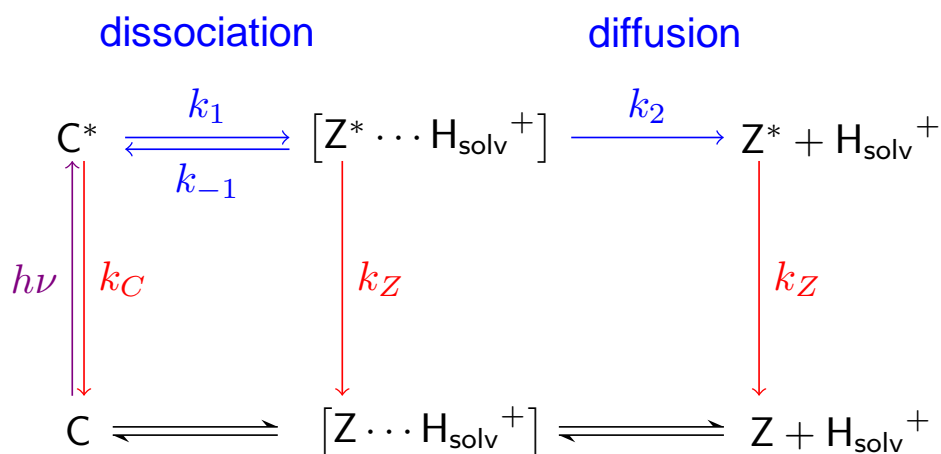
Scheme 2: Photodissociation mechanism of **C*** in hydroxylic solvents. Deactivation processes are indicated in red and elementary stages of the proton transfer reactions in blue.
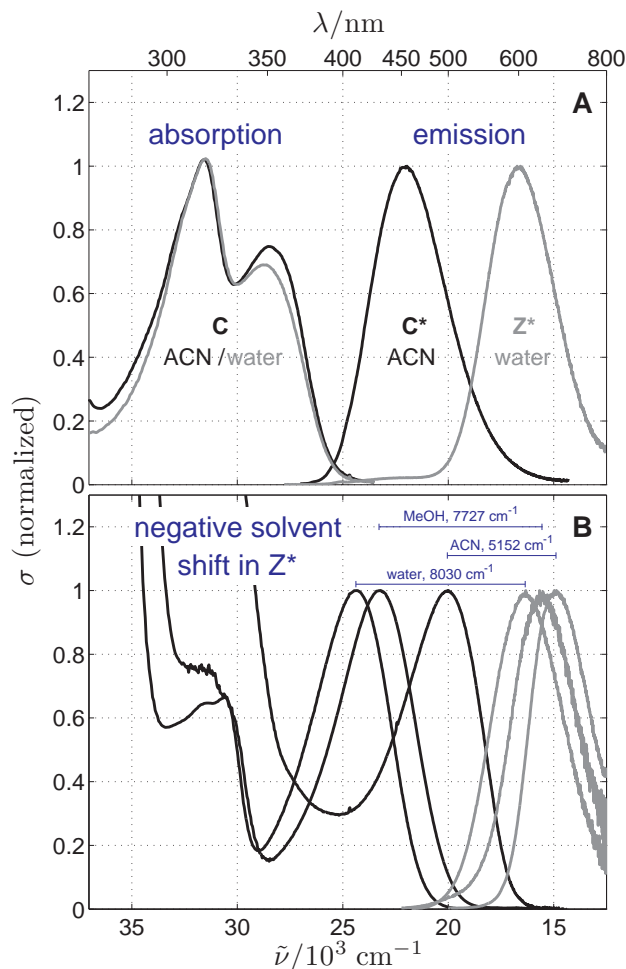
Figure 1: Frame A: normalized absorption and stimulated emission cross-sections (σ) of the N−methyl−6−hydroxyquinolinium cation (**C** form) in water (pH=4, gray) and acetonitrile (black). The red-shifted emission observed in water ($\lambda_{max} \approx 600$ nm) indicates photoinduced proton transfer to solvent. Frame B: normalized cross-sections of absorption (black) and SE (gray) of the neutral form N−methylquinolinium−6−olate (**Z**) in methanol (MeOH), acetonitrile (ACN) and water. The inset shows the Stokes shift in reciprocal centimeters. Negative solvatochromism is observed, *i.e.* a decrease of dipole moment of the neutral form upon excitation.
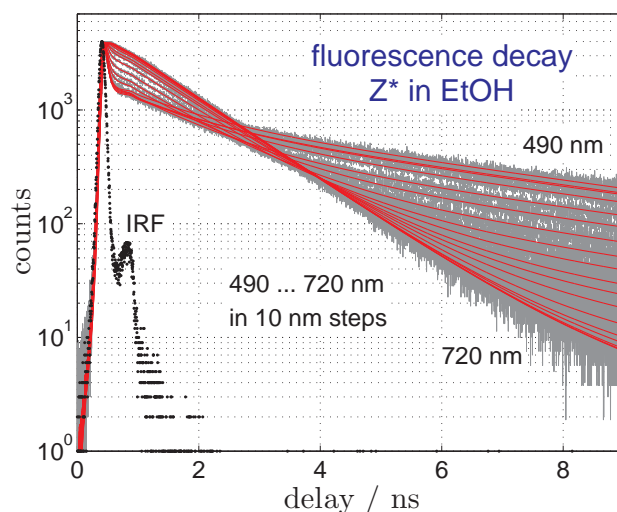
Figure 2: Fluorescence decay curves of the neutral form ($\mathbf{Z}^*$) measured in EtOH between 490 and 720 nm in 10 nm steps (gray). The instrument response function (IRF, FWHM $\approx$ 100 ps) is represented by black dots. Red lines result from global multi-exponential fits.
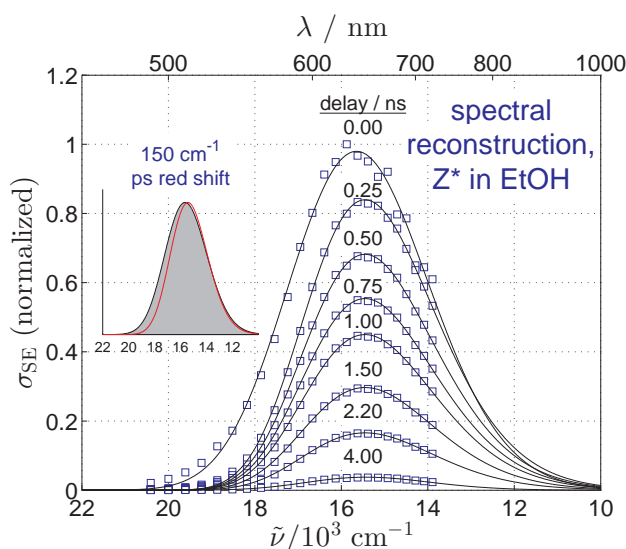

Figure 3: Reconstruction of the stimulated emission spectrum observed upon excitation of the neutral form $\mathbf{Z}$ in EtOH. Experimental points (blue squares) are obtained from TC-SPC fluorescence decay data and converted to stimulated emission cross-section. Solid lines represent *log-normal* fits at each delay time. Delay times are indicated by labels close to each spectrum. The inset shows the first (black, gray filled) and last (red, 4 ns delay) reconstructed spectra, as obtained by ps fluorescence. A redshift of $\approx 150\ \mathrm{cm}^{-1}$ is observed during the earliest 250 ps.
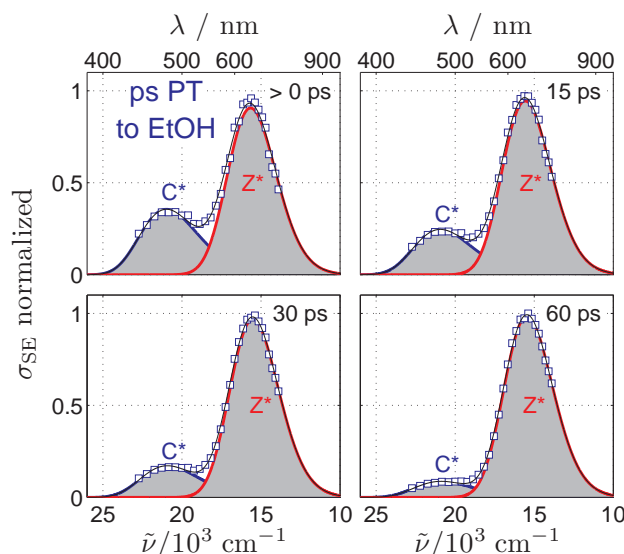
Figure 4: Reconstruction of the stimulated emission spectrum obtained upon ps excitation of the cationic form **C** in EtOH. Experimental points (blue squares) result from transforming TC-SPC data into stimulated emission cross-section. The resulting spectrum is fitted to a sum of two *log-normal* functions (thin black solid line) accounting for the individual cross-sections of the neutral ($\mathbf{Z}^*$, red) and cationic ($\mathbf{C}^*$, blue) forms. The time delays are indicated. Spectra were normalized to a value of 1 at the maximum. On the ps timescale, a significant amount of $\mathbf{Z}^*$ forms impulsively. Slow (ps) decay of $\mathbf{C}^*$ and concomitant rise of $\mathbf{Z}^*$ is observed.
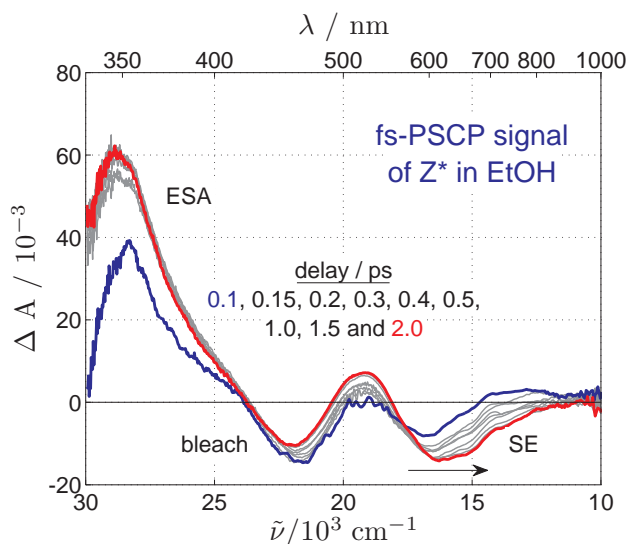

Figure 5: fs transient absorption spectra of $\mathbf{Z}^*$ in EtOH measured with parallel pump-probe polarization. Excited-state absorption (ESA) and stimulated emission (SE) contributions are labeled. Pump-probe delays are indicated. The arrow shows the direction of spectral evolution towards longer delays. Undulations in the SE band reflect underlying wavepacket motion.
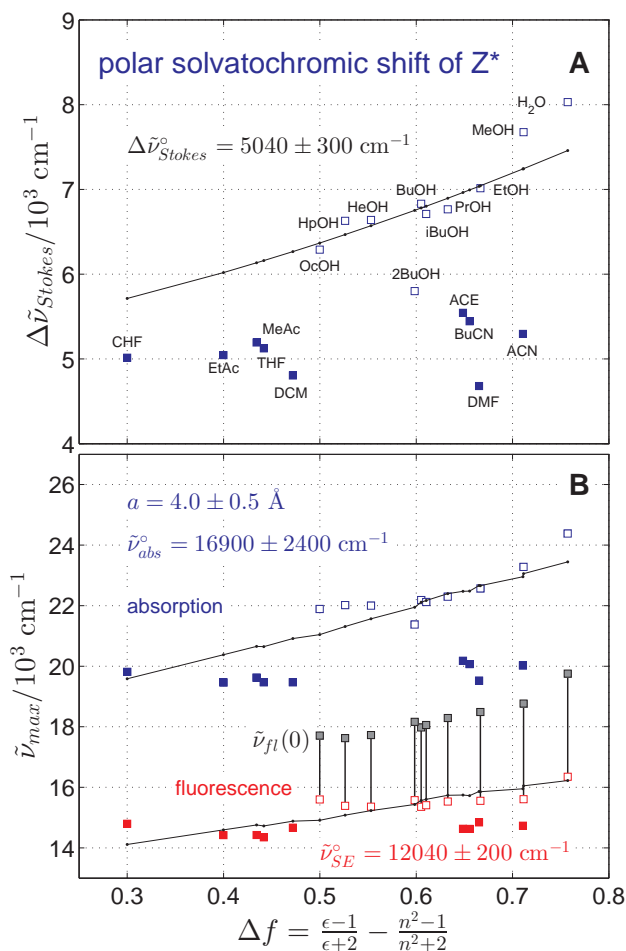
Figure 6: Analysis of the polar solvatochromic shift of $\mathbf{Z}^*$. Frame A: dependence of the Stokes shift (cm^{-1}) on the solvent polarity parameter $\Delta f(\varepsilon, n^2)$ for non-protic (filled blue squares) and protic solvents (empty blue squares). The solvatochromic shift in polar protic solvents is simulated with the classical theory of solvatochromism and molecular properties derived from quantum chemical calculations (thin solid line and dots). The following values were used: $\mu_0 = 10.5$ D, $\mu_1 = 7.3$ D, $\alpha_0 = 22.3$ Å^3 and $\alpha_1 = 18.4$ Å^3. The fitted gas-phase Stokes shift $\Delta\tilde{\nu}^\circ_{Stokes}$ is indicated. Solvents are identified by labels close to each data point. Frame B: absorption (blue squares) and stimulated emission (SE, red squares) peak positions as function of the solvent polarity parameter. Filled and empty symbols differentiate between non-protic and protic solvents, respectively. Peak positions are simulated semiquantitatively by the dielectric continuum theory of solvatochromism (thin solid line and dots) for protic solvents only. Non-protic solvents deviate markedly. The SE peak positions at time zero (gray-filled squares, $\tilde{\nu}_{fl}(0)$) are estimated by adding the orientational contribution to the experimental peak positions, see text. The optimal values for the gas-phase absorption $\tilde{\nu}^\circ_{abs}$ and SE $\tilde{\nu}^\circ_{SE}$ peaks are indicated together with the cavity radius a. The vertical lines gauge the extent of the dynamic Stokes shift in polar protic solvents.
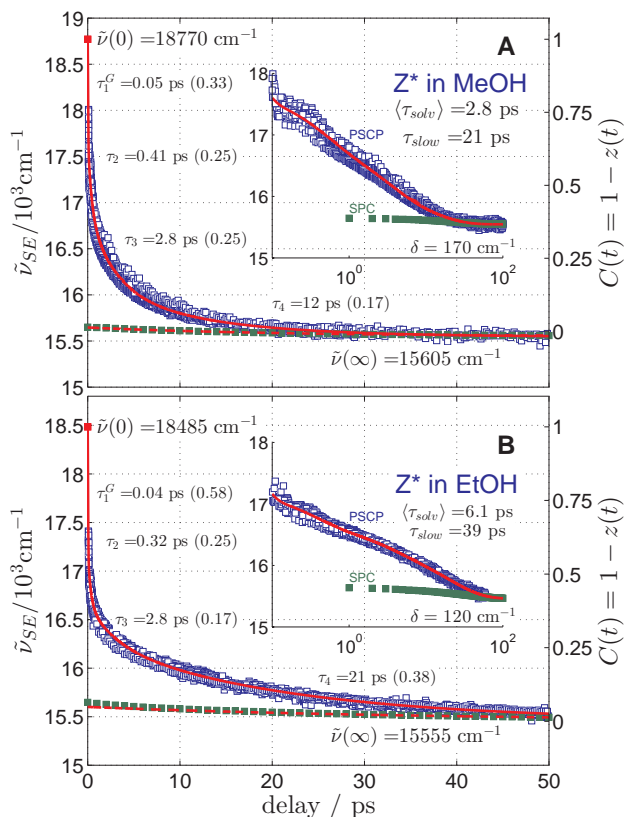
Figure 7: The dynamic red-shift of the $\mathbf{Z}^*$ SE band is used to monitor solvation dynamics in MeOH (panel A) and EtOH (panel B). In the femtosecond timescale, peak positions are measured by PSCP spectroscopy (blue squares). Slower dynamics is reconstructed from ps TC-SPC (green squares). The peak positions at times zero and infinitum ($\tilde{\nu}(0)$ and $\tilde{\nu}(\infty)$) are estimated by the analysis of solvatochromic shifts with dielectric continuum theory. This is then used to obtain the solvation correlation function ($C(t)$, red solid line), which is fitted with three exponentials and a Gaussian function. Decay times (τ_i) and associated amplitudes are indicated as inset together with average solvation times ($\langle \tau_{solv} \rangle$) and the slowest decay obtained by TC-SPC (τ_{slow}). The inner graphs represent the same datasets on a logarithmic scale.
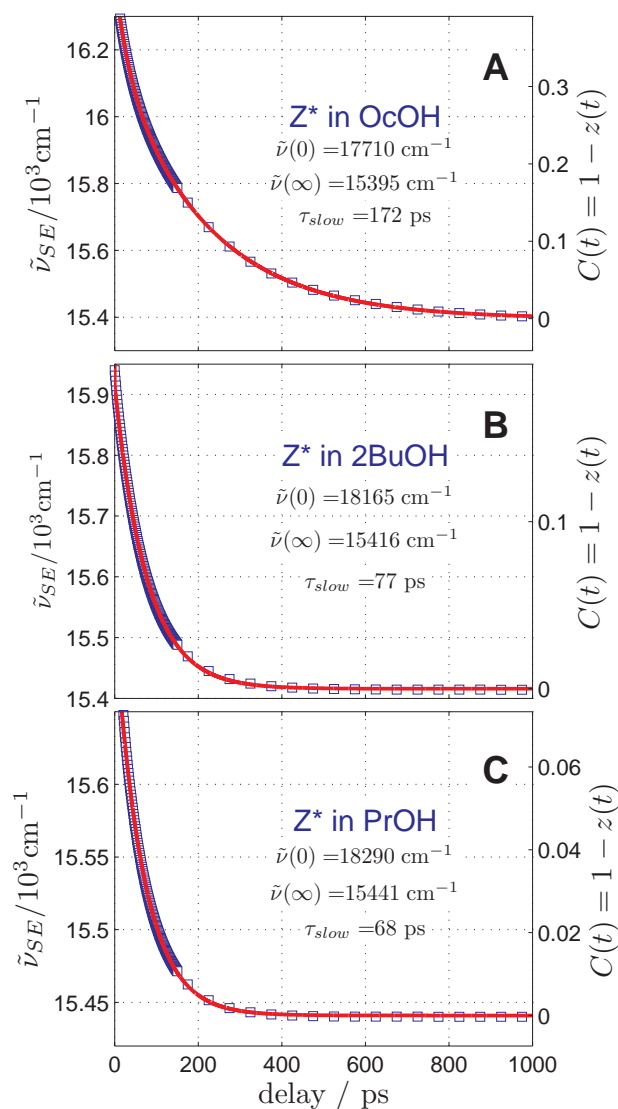
Figure 8: Picosecond time-evolution of the $\mathbf{Z}^*$ SE peak position ($\tilde{\nu}_{\text{SE}}$ blue squares) in OcOH (Panel A), 2BuOH (B) and PrOH (C). The peak position was obtained by spectral reconstruction of TC-SPC data. The analysis of the solvatochromic shift is used to predict the peak position of the SE band at time zero, $\tilde{\nu}(0)$. The latter is necessary for calculating the solvation correlation function $C(t)$, shown on the right axes. $C(t)$ monitors the rate of energy dissipation in the solvation coordinate $z(t)$. The peak position is fitted with monoexponential (PrOH and 2BuOH) or bi-exponential (OcOH) functions and an offset. The characteristic time (τ_{slow}) is indicated as inset. Note that $\tilde{\nu}(\infty)$ is obtained from the fitting procedure as the offset amplitude. Deviations from the steady-state SE peak position are less than our spectral resolution of $200\ \text{cm}^{-1}$.

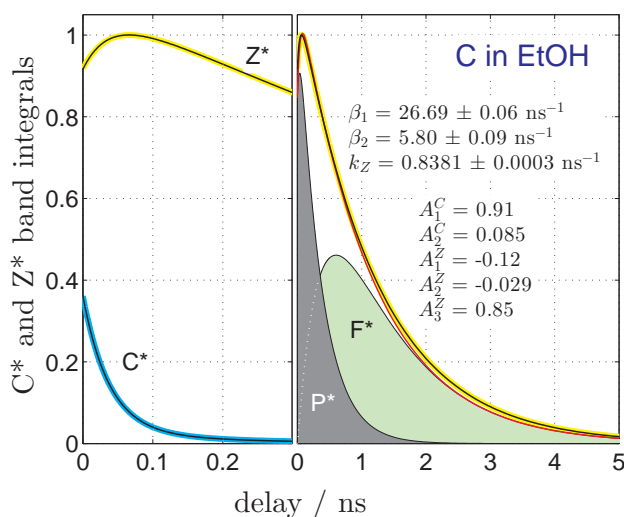Figure 9: Picosecond time-evolution of the $\mathbf{C}^*$ (cyan) and $\mathbf{Z}^*$ (yellow) SE band integrals measured upon $\mathbf{C}$ excitation in EtOH. The left frame shows the evolution of both band integrals during the earliest 300 ps, as measured with ps time resolution. The right frame shows the complete evolution of $\mathbf{Z}^*$. Band integrals were fitted globally with biexponential ($\mathbf{C}^*$) and triexponential ($\mathbf{Z}^*$) functions, as deduced from the model in Scheme 1. The decay constants (β_1, β_2 and k_Z) are indicated together with the associated amplitudes. The fits are shown as black solid lines. Red solid lines represent the same global fit with amplitudes constrained to the analytical forms derived from the kinetic model in Scheme 1. This provides the time-evolution of $\mathbf{Z}^*$ concentration in the encounter complex ($\mathbf{P}^*$, gray-filled curve) and of free $\mathbf{Z}^*$ ($\mathbf{F}^*$, light green-filled curve).
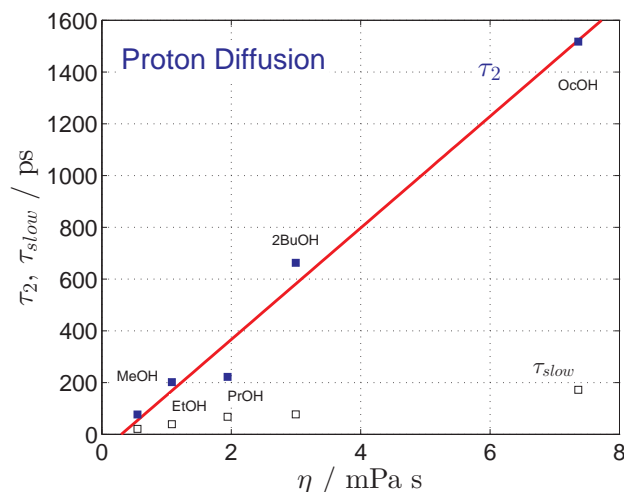
Figure 10: Linear dependence of the proton-diffusion time constant (τ_2, blue-filled squares) on solvent viscosity η. The red solid line shows the linear fit. τ_2 is compared with the slowest solvation components determined by analysis of $\mathbf{Z}^*$ solvation dynamics (black empty squares).

1
2
3
4
5
6
7
8
9
10
11
12
13
14
15
16
17
18
19
20
21
22
23
24
25
26
27
28
29
30
31
32
33
34
35
36
37
38
39
40
41
42
43
44
45
46
47
48
49
50
51
52
53
54
55
56
57
58
59
60

Table of Contents, TOC

dissociation of a strong acid in alcohols
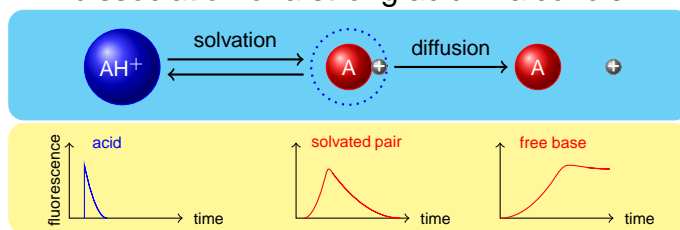
Supporting Information of "Dissociation of a Strong Acid in Neat Solvents: Diffusion is Observed after Reversible Proton Ejection inside the Solvent Shell."

M. Veiga-Gutiérrez,[†,¶] Alfonso Brenlla,[†,§] C. Carreira Blanco,[†] Berta Fernández,[†] Sergey A. Kovalenko,[‡] Flor Rodríguez Prieto,[†] M. Mosquera,[*,†] and J. Luis Pérez Lustres[*,†]

Center for Research in Biological Chemistry and Molecular Materials (CIQUS), University of Santiago de Compostela, E-15782 Santiago de Compostela (Spain), and Institute of Chemistry, Humboldt University of Berlin, D-12489 Berlin (Germany)

E-mail: manuel.mosquera@usc.es; luis.lustres@usc.es

---

[*]To whom correspondence should be addressed
[†]CIQUS
[‡]HUB
[¶]now at PicoQuant GmbH, Kekuléstr. 7, 12489 Berlin (Germany)
[§]now at Department of Chemistry, Wayne State University, 5101 Cass Avenue, Detroit, MI 48202 (USA)

Quantum Chemical Calculations
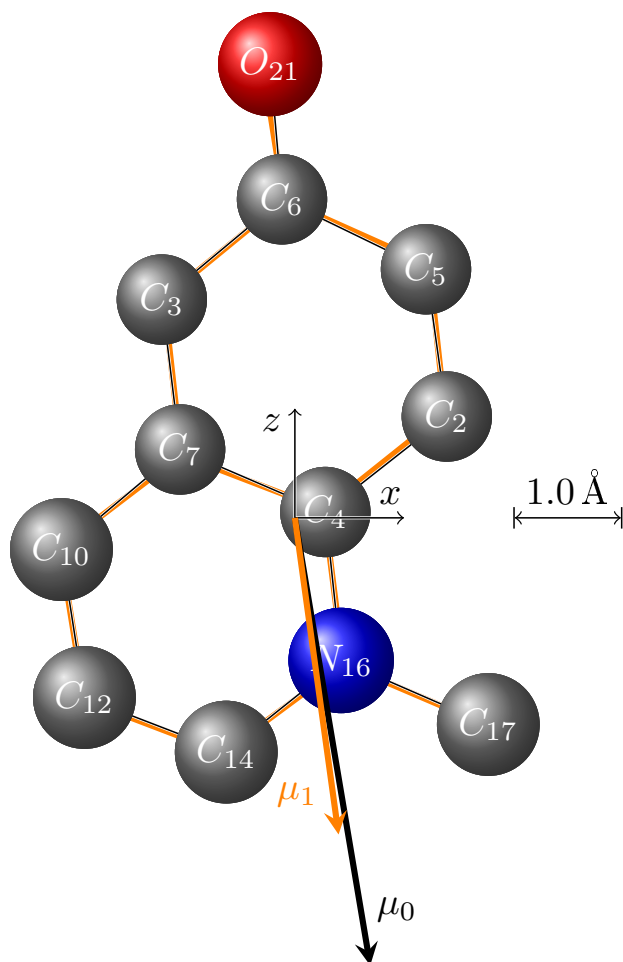
Figure SI 1: Atom numbering and geometries of the ground (black sticks) and first-excited singlet state (orange). Hydrogens were omitted. Dipole moments of both states are shown with the same color code, as indicated by the legends. They are nearly parallel to the O–N line. The molecular size is given by the gauge shown in the inset. The molecule is calculated to be planar in both states and lays on the *xz* plane, as specified by the axis.

Table SI 1: Ground-state molecular electrical properties of **Z** obtained from quantum chemical calculations. The geometries were optimized with the indicated methods and bases. Only non-zero components are listed.

method	μ/ D	μ_x/a.u.	μ_z/a.u.	$\bar{\alpha}$/Å^3	α_{xx}/a.u.	α_{yy}/a.u.	α_{xz}/a.u.	α_{zz}/a.u.
			S_0, cc-pVTZ basis set, B3LYP//cc-pVTZ geometry					
HF	11.858	0.705	−4.612	20.30	139.45	60.66	22.69	210.89
B3LYP	10.226	0.696	−3.962	20.70	142.44	60.84	18.88	215.70
			S_0, aug-cc-pVTZ basis set, B3LYP//cc-pVTZ geometry					
HF	12.008	0.694	−4.673	19.26	145.08	73.19	23.37	221.57
B3LYP	10.500	0.693	−4.072	22.33	149.04	73.62	19.39	229.42
			S_0, 6-311+G** basis set, B3LYP//cc-pVTZ geometry					
B3LYP	10.707	0.727	−4.149	21.64	143.19	69.12	20.28	225.71
			S_0, cc-pVTZ basis set, B3LYP//aug-cc-pVTZ geometry					
HF	11.917	0.703	−4.635	20.29	139.40	60.66	22.58	210.65
B3LYP	10.264	0.696	−3.978	20.70	142.41	60.83	18.87	215.85
			S_0, aug-cc-pVTZ basis set, B3LYP//aug-cc-pVTZ geometry					
HF	12.070	0.692	−4.698	19.24	145.02	73.17	23.25	221.31
B3LYP	10.542	0.693	−4.089	22.34	149.01	73.62	19.38	229.62

Table SI 2: B3LYP molecular electrical properties obtained at the S_1 excited state B3LYP/aug-cc-pVTZ optimized geometry of **Z**.

State	basis set	μ/D	μ_x/a.u.	μ_y/a.u.	μ_z/a.u.
S_0	cc-pVTZ	10.812	0.695	0.000	−4.197
	aug-cc-pVTZ	11.137	0.691	0.000	−4.327
S_1	cc-pVTZ	7.191	0.375	0.000	−2.804
	aug-cc-pVTZ	7.326	0.403	0.000	−2.854

State	basis set	$\bar{\alpha}$/Å^3	α_{xx}/a.u.	α_{yy}/a.u.	α_{zz}/a.u.
S_0	cc-pVTZ	21.02	147.22	61.14	217.19
	aug-cc-pVTZ	22.68	153.78	74.18	231.17
S_1	cc-pVTZ	18.36	138.90	62.53	170.27
	aug-cc-pVTZ	20.08	148.31	77.95	180.33

Table SI 3: Basis set and method selection for the ground state geometry optimization: Summary of the main results. Internal coordinates in Å and degrees. Atom numbering shown in Figure SI 1.

Parameter	B3LYP/aug-cc-pVTZ (cc-pVTZ)	HF/aug-cc-pVTZ (cc-pVTZ)	MP2/(cc-pVTZ)
R(2,4)	1.415 (1.415)	1.421 (1.422)	(1.411)
R(2,5)	1.362 (1.362)	1.344 (1.344)	(1.371)
R(3,6)	1.433 (1.435)	1.420 (1.422)	(1.441)
R(3,7)	1.383 (1.382)	1.382 (1.380)	(1.379)
R(4,7)	1.448 (1.449)	1.427 (1.428)	(1.455)
R(4,16)	1.368 (1.367)	1.357 (1.356)	(1.363)
R(5,6)	1.466 (1.467)	1.470 (1.471)	(1.464)
R(6,21)	1.242 (1.239)	1.218 (1.217)	(1.242)
R(7,10)	1.422 (1.423)	1.416 (1.417)	(1.423)
R(10,12)	1.371 (1.371)	1.360 (1.360)	(1.375)
R(12,14)	1.392 (1.392)	1.386 (1.386)	(1.395)
R(14,16)	1.346 (1.347)	1.320 (1.320)	(1.352)
R(16,17)	1.470 (1.470)	1.465 (1.464)	(1.465)
A(4,2,5)	120.1 (120.1)	120.2 (120.2)	(119.6)
A(6,3,7)	122.9 (123.0)	122.4 (122.5)	(122.9)
A(2,4,7)	118.5 (118.5)	118.0 (117.9)	(118.9)
A(2,4,16)	122.1 (122.1)	122.1 (122.1)	(121.9)
A(2,5,6)	124.0 (124.0)	124.1 (124.1)	(124.4)
A(3,6,5)	114.3 (114.1)	114.2 (114.1)	(114.0)
A(3,6,21)	124.8 (124.9)	125.5 (125.6)	(124.7)
A(3,7,4)	120.2 (120.3)	121.2 (121.2)	(120.2)
A(3,7,10)	123.2 (123.2)	122.6 (122.7)	(123.2)
A(7,10,12)	121.3 (121.3)	121.3 (121.3)	(121.3)
A(10,12,14)	119.9 (119.9)	119.5 (119.5)	(120.1)
A(12,14,16)	120.4 (120.3)	120.7 (120.6)	(119.9)
A(4,16,14)	122.5 (122.5)	122.4 (122.5)	(123.0)
A(4,16,17)	119.6 (119.6)	119.6 (119.6)	(119.1)

Table SI 4: B3LYP/aug-cc-pVTZ optimized geometries for the ground state. Cartesian coordinates in Å. Atom numbering shown in Figure SI 1.

Atom	x	y	z
1	2.398127	0.000000	0.536729
2	1.391518	0.000000	0.927706
3	-1.218478	0.000000	1.999001
4	0.279378	0.000000	0.053309
5	1.200983	0.000000	2.276361
6	-0.117813	0.000000	2.916996
7	-1.051006	0.000000	0.626007
8	2.052747	0.000000	2.944407
9	-2.218336	0.000000	2.412810
10	-2.138035	0.000000	-0.290770
11	-3.145291	0.000000	0.103717
12	-1.927402	0.000000	-1.645356
13	-2.751401	0.000000	-2.343207
14	-0.628565	0.000000	-2.145649
15	-0.406202	0.000000	-3.199189
16	0.423939	0.000000	-1.306496
17	1.771596	0.000000	-1.892973
18	2.315484	-0.887367	-1.577281
19	2.315484	0.887367	-1.577281
20	1.679954	0.000000	-2.973379
21	-0.226682	0.000000	4.154539

Table SI 5: B3LYP/aug-cc-pVTZ optimized geometries for the first excited singlet state. Cartesian coordinates in Å. Atom numbering shown in Figure SI 1.

Atom	x	y	z
1	2.375381	-0.000111	0.551881
2	1.375485	-0.000077	0.961894
3	-1.199671	-0.000278	2.008354
4	0.265445	0.000016	0.075513
5	1.227296	-0.000252	2.317138
6	-0.099141	-0.000353	2.910207
7	-1.040648	-0.000089	0.575967
8	2.080169	-0.000307	2.978955
9	-2.193888	-0.000251	2.432682
10	-2.152416	0.000053	-0.271620
11	-3.150859	0.000137	0.137233
12	-1.926648	0.000164	-1.668201
13	-2.747596	0.000355	-2.369236
14	-0.656360	0.000097	-2.152420
15	-0.449624	0.000138	-3.211994
16	0.444334	0.000018	-1.336617
17	1.775525	0.000198	-1.906090
18	2.336177	-0.886494	-1.600103
19	2.336664	0.885935	-1.598297
20	1.696605	0.001351	-2.989564
21	-0.296233	-0.000255	4.154322

Time-Dependent Concentrations

Analytical expressions for the time-dependent concentrations resulting from the kinetic model in Scheme 2 were derived by matrix algebra. The definitions in Equations (SI.1) were employed to simplify the final expressions. The initial conditions are specified in Equations (SI.2). Remember that non-zero initial concentration of the $\mathbf{P}^*$ form is explained by the unresolved stages of solvation.

$$X = k_1 + k_C \tag{SI.1a}$$

$$Y = k_2 + k_Z + k_{-1} \tag{SI.1b}$$

$$Z = \sqrt{(X-Y)^2 + 4k_1 k_{-1}} \tag{SI.1c}$$

$$\beta_1 = \frac{1}{2}(X+Y+Z) \tag{SI.1d}$$

$$\beta_2 = \frac{1}{2}(X+Y-Z) \tag{SI.1e}$$

$$\Delta = Y \cdot k_Z - XY + k_1 \cdot k_{-1} \tag{SI.1f}$$

$$[\mathrm{C}^*](0) = C_0 \tag{SI.2a}$$

$$[\mathrm{P}^*](0) = Z_0 \tag{SI.2b}$$

$$[\mathrm{F}^*](0) = 0 \tag{SI.2c}$$

The resulting time-dependent concentrations of the species involved are collected in Equations (SI.3).

$$[C^*(t)] = \frac{1}{k_1(\beta_1 - \beta_2)(\Delta + Xk_Z - k_Z^2)} \times$$

$$\{[\Delta + \beta_1(X - k_Z)][C_0 k_1(\beta_2 - k_Z) + Z_0(\Delta + X\beta_2 - k_Z\beta_2)]e^{-\beta_1 t}$$

$$+ [\Delta + \beta_2(X - k_Z)][C_0 k_1(\beta_1 - k_Z) + Z_0(\Delta + X\beta_1 - k_Z\beta_1)]e^{-\beta_2 t}\}$$

(SI.3a)

$$[P^*(t)] = \frac{1}{(\beta_1 - \beta_2)(\Delta + Xk_Z - k_Z^2)} \times$$

$$\{(\beta_1 - k_Z)[C_0 k_1(\beta_2 - k_Z) + Z_0(\Delta + X\beta_2 - k_Z\beta_2)]e^{-\beta_1 t}$$

$$- (\beta_2 - k_Z)[C_0 k_1(\beta_1 - k_Z) + Z_0(\Delta + X\beta_1 - k_Z\beta_1)]e^{-\beta_2 t}\}$$

(SI.3b)

$$[F^*(t)] = \frac{1}{(\Delta + Xk_Z - k_Z^2)} \times$$

$$\{-\frac{k_2}{\beta_1 - \beta_2}[C_0 k_1(\beta_2 - k_Z) + Z_0(\Delta + X\beta_2 - k_Z\beta_2)]e^{-\beta_1 t}$$

$$+ \frac{k_2}{\beta_1 - \beta_2}[C_0 k_1(\beta_1 - k_Z) + Z_0(\Delta + X\beta_1 - k_Z\beta_1)]e^{-\beta_2 t}$$

$$- k_2[C_0 k_1 + Z_0(X - k_Z)]e^{-k_Z t}\}$$

(SI.3c)

$$[Z^*(t)] = [P^*(t)] + [F^*(t)]$$

(SI.3d)

The small contribution of the second exponential in the decay of **C*** indicates that $k_{-1} \ll k_1 + k_2 + k_Z$. Therefore, it can be deduced that

$$\beta_1 + \beta_2 = k_1 + k_2 + k_Z + k_{-1} \approx k_1 + k_2 + k_Z \qquad \text{(SI.4a)}$$

$$\beta_1 \times \beta_2 = k_1(k_2 + k_Z) \qquad \text{(SI.4b)}$$

Stimulated Emission Band Integrals of Z*
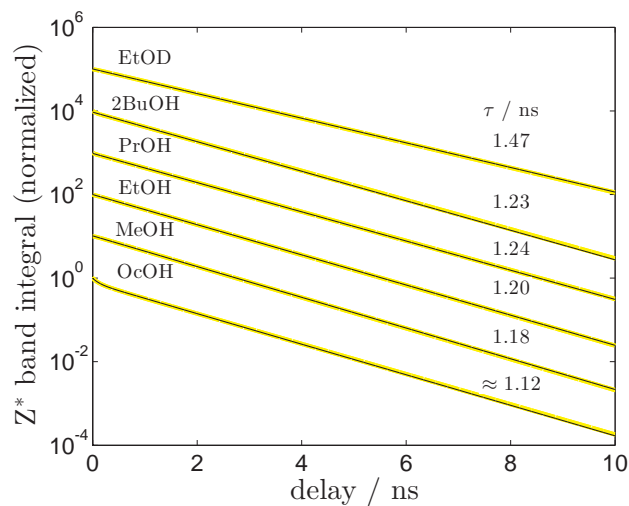
Figure SI 2: Time evolution of the **Z*** stimulated emission band integrals (thick yellow lines) measured in the various alcohols. A monoexponential fit is shown, thin solid line, and the decay time is indicated. Only 1-octanol shows a minor contribution of a second short exponential (20%).

Global Multiexponential Fit of the Time-Resolved Fluorescence of C* in Ethanol
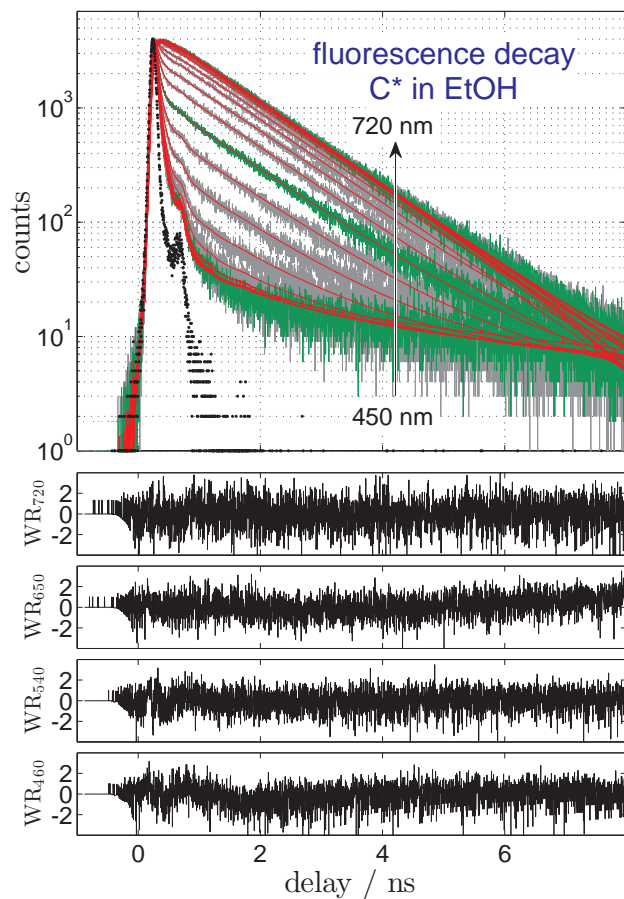
Figure SI 3: Fluorescence decay curves (gray) measured between 450 and 720 nm for C* in ethanol. Four-exponential global fits are shown as red lines while the IRF is represented by black dots. Weighted residuals (WR) resulting from the global fit are shown in the lower panels for some representative wavelengths (indicated by green decay curves in the upper panel). All χ_N^2 values are below 1.2.

PTTS in Ethanol Shown on a Logarithmic Scale

The logarithmic representation in Figure SI 4 clearly exposes the non-exponential decay of $\mathbf{C}^*$ in ethanol. Similar results are obtained in other alcohols. In addition, decay and rise of $\mathbf{C}^*$ and $\mathbf{Z}^*$, respectively, occur at different rates. Consequently, a global biexponential fit yields good results for the cation but deviates slightly for the reaction product. Biexponential decay of $\mathbf{C}^*$ and triexponential evolution of $\mathbf{Z}^*$ fit the data up to noise level and yield rate constants which are consistent with independent measurements of solvation dynamics and $\mathbf{Z}^*$ deactivation, see main text.
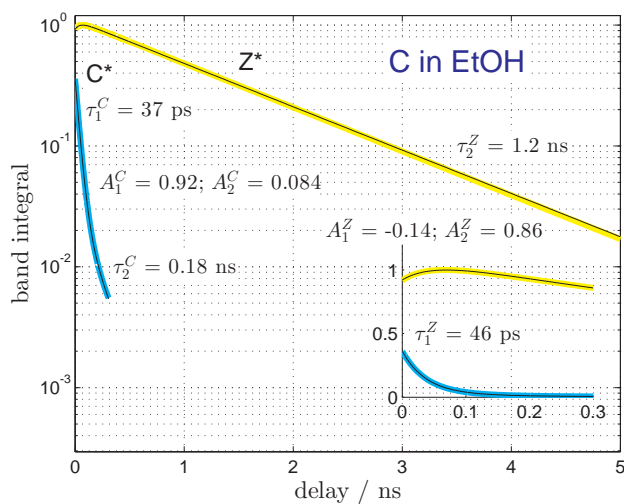
Figure SI 4: Logarithmic representation of the picosecond time-evolution of $\mathbf{C}^*$ (cyan solid line) and $\mathbf{Z}^*$ (yellow solid line) SE band integrals. Measurements performed upon $\mathbf{C}$ excitation in EtOH. Both band integrals were fitted globally with biexponential functions (thin solid lines). The inset zooms the earliest 0.3 ns on a linear scale. Decay constants and associated amplitudes are indicated.

11

PTTS in 1-Octanol
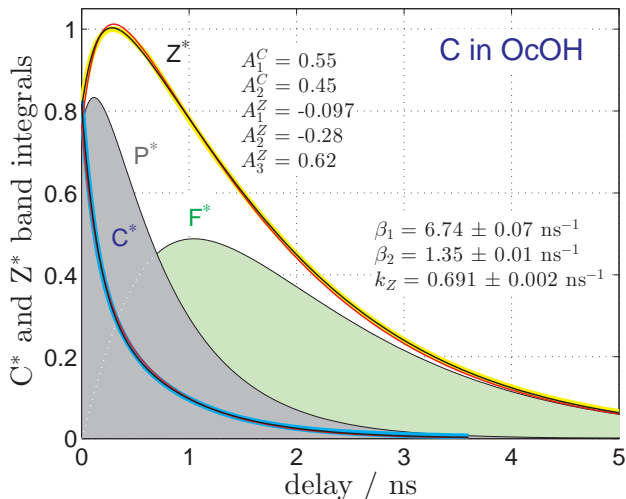
Figure SI 5: Picosecond time-evolution of the **C*** (cyan solid line) and **Z*** (green solid line) SE band integrals measured upon **C** excitation in OcOH. Band integrals were fitted globally with biexponential (**C***) and triexponential (**Z***) functions, as deduced from the model in Scheme 2. The decay constants (β_1, β_2 and k_Z) are indicated together with the associated amplitudes. The fits are shown as black solid lines. Red solid lines represent the same global fit with amplitudes constrained to the analytical forms derived from the kinetic model in Scheme 2, Equations (SI.3). This provides the time-evolution of **Z*** concentration in the encounter complex (**P***, gray-filled curve) and free (**F***, light green-filled curve).

Solvent Abbreviations

The following abbreviations were used for the solvents employed in this work: ACE (acetone), ACN (acetonitrile), BuCN (butyronitrile), BuOH (1-butanol), 2BuOH (2-butanol), CHF (chloroform), DCM (dichloromethane), DMF (dimethylformamide), EtAc (ethyl acetate), EtOH (ethanol), HeOH (1-hexanol), HpOH (1-heptanol), iBuOH (i-butanol), MeAc (methyl acetate), MeOH (methanol), OcOH (1-octanol), PrOH (1-propanol), THF (tetrahydrofurane) and WAT (water).

Gaussian 09, Full Reference

M. J. Frisch, G. W. Trucks, H. B. Schlegel, G. E. Scuseria, M. A. Robb, J. R. Cheeseman, G. Scalmani, V. Barone, B. Mennucci, G. A. Petersson, H. Nakatsuji, M. Caricato, X. Li, H. P. Hratchian, A. F. Izmaylov, J. Bloino, G. Zheng, J. L. Sonnenberg, M. Hada, M. Ehara, K. Toyota, R. Fukuda, J. Hasegawa, M. Ishida, T. Nakajima, Y. Honda, O. Kitao, H. Nakai, T. Vreven, Montgomery, Jr., J. A., J. E. Peralta, F. Ogliaro, M. Bearpark, J. J. Heyd, E. Brothers, K. N. Kudin, V. N. Staroverov, R. Kobayashi, J. Norm, K. Raghavachari, A. Rendell, J. C. Burant, S. S. Iyengar, J. Tomasi, M. Cossi, N. Rega, J. M. Millam, M. Klene, J. E. Knox, J. B. Cross, V. Bakken, C. Adamo, J. Jaramillo, R. Gomperts, R. E. Stratmann, O. Yazyev, A. J. Austin, R. Cammi, C. Pomelli, J. W. Ochterski, R. L. Martin, K. Morokuma, V. G. Zakrzewski, G. A. Voth, P. Salvador, J. J. Dannenberg, S. Dapprich, A. D. Daniels, Ö. Farkas, J. B. Foresman, J. V. Ortiz, J. Cioslowski. D. J. Fox, Gaussian 09 Revision A.1, Gaussian Inc. Wallingford CT 2009.